# Elevator mechanism dynamics in a sodium-coupled dicarboxylate transporter

Kinz-Thompson, C.D.,[1,†] Lopez-Redondo, M.L.,[2,‡] Mulligan C.,[3] Sauer, D.B.,[2,§] Marden, J.J.,[2] Song, J.,[2] Tajkhorshid, E.,[4] Hunt, J.F.,[5] Stokes, D.L.,[2] Mindell, J.A.,[6*] Wang, D.N,[2*] Gonzalez, Jr., R.L.[1*]

1. Department of Chemistry, Columbia University, New York, New York 10027, US
2. Department of Cell Biology, New York University School of Medicine, New York, New York 10016, US
3. School of Biosciences, University of Kent, Canterbury, Kent, CT2 7NH, UK
4. Theoretical and Computational Biophysics Group, NIH Center for Macromolecular Modeling and Bioinformatics, Beckman Institute for Advanced Science and Technology, Department of Biochemistry, Center for Biophysics and Quantitative Biology, University of Illinois at Urbana-Champaign, Urbana, IL 61801, US
5. Department of Biological Sciences, Columbia University, New York, New York 10027, US
6. Membrane Transport Biophysics Section, Porter Neuroscience Research Center, National Institute of Neurological Disorders and Stroke, National Institutes of Health, Bethesda, MD 20892, US

*Correspondence: rlg2118@columbia.edu, da-neng.wang@med.nyu.edu, mindellj@ninds.nih.gov
†Current address: Department of Chemistry, Rutgers University-Newark, Newark, New Jersey 07012, US
‡Current address: Instituto de Biomedicina de Valencia, Consejo Superior de Investigaciones Científicas (IBV-CSIC), 46010 Valencia, Spain
§Current address: Centre for Medicines Discovery, Nuffield Department of Medicine, University of Oxford, Oxford, OX1 3QU, UK

## Abstract

VcINDY, the sodium-dependent dicarboxylate transporter from *Vibrio cholerae*, is responsible for $C_4$- and $C_5$-carboxylate uptake into cells. The molecular mechanism of how VcINDY physically moves substrates across the membrane, and does so in an energetically efficient manner, is unclear. Here, we use single-molecule fluorescence resonance energy transfer experiments to directly observe the individual mechanistic steps that VcINDY takes to translocate substrates across a lipid bilayer, and then test key predictions of transport cycle mechanistic models. Our data provide the first direct evidence that VcINDY undergoes stochastic, elevator-type conformational motions that enable substrate translocation. Kinetic analysis suggests that the two protomers of the VcINDY homodimer undergo those motions in a non-cooperative manner, and thus catalyze two independent transport reactions. The relative substrate independence of those motions supports the notion that the VcINDY transport cycle maintains strict co-substrate coupling using a cooperative binding mechanism. Finally, thermodynamic modeling provides insight into how such a cooperative binding mechanism provides a generalized approach to optimizing transport for many secondary active transporters.

# Introduction

Secondary active transporters are transmembrane proteins that harvest free energy from electrochemical gradients to drive the movement of substrates across a membrane (Fig. 1) (Stein and Lieb, 1986). In the absence of a free energy source, these transporters move substrates back and forth across the membrane without creating a net change in substrate concentration (Jardetzky, 1966). Net transport occurs because the transporter can dissipate the electrochemical gradient of a 'driving' substrate to harvest free energy, and then couple that free energy to the 'uphill' movement of a 'driven' substrate across the membrane (Forrest et al., 2011). The mechanistic details of this coupling are governed by the transport cycle, which describes how the transporter binds its substrates, translocates them across the membrane, releases them, and resets itself for the next round (Fig. 1B). While the specific details of the transport cycle and how it is achieved on a molecular level are unique to each transporter or transporter family, the active use of free energy suggests that transport cycles must maintain strict substrate coupling to minimize energetically wasteful 'slippage cycles' (*c.f.*, Fig. 1B) in which driving substrates are transported without driving the translocation of the driven substrate (Stein and Lieb, 1986).

While all secondary active transporters work by facilitating a general, dynamic equilibrium (*e.g.*, $mA_{\text{outside}} + nB_{\text{outside}} \rightleftharpoons mA_{\text{inside}} + nB_{\text{inside}}$, where $A$ and $B$ are co-substrates with stoichiometries $m$ and $n$), the molecular details of how this chemical reaction maps on to the transport cycle are determined by a transporter's conformational dynamics. According to the alternating access hypothesis, secondary active transporters must undergo a reversible conformational transition between at least two distinct conformational states: one with the substrate binding pocket in a state that is 'outward-facing' with respect to membrane ($C_o$), and one in an 'inward-facing' state ($C_i$) (Jardetzky, 1966). While there are many possible structural implementations of alternating access, including the so-called 'rocker-switch', 'rocking-bundle', and 'elevator' transport mechanisms (Drew and Boudker, 2016), at least two distinct conformational transitions between $C_i$ and $C_o$ must occur in a complete transport cycle (*c.f.*, Fig. 1B). Here, we investigate the role of such conformational dynamics in the transport cycle of the prototypical sodium-dependent divalent anion transporter from mesophilic *Vibrio cholerae*, VcINDY, and elucidate how they are tuned to enable efficient transport and minimize slippage.

VcINDY is a well-characterized member of the divalent anion/sodium symporter (DASS) class of secondary active transporters, which extends across all kingdoms of life. In mammals, it is represented by the solute carrier 13 (SLC13) gene family, which includes members that transport di- and trivalent anions, including sulfate, citrate, and succinate (Bergeron et al., 2013; Markovich, 2012). Within this family, the SLC13A5 citrate transporter, NaCT, has significant metabolic and neurologic health importance for humans, and mutations in NaCT can cause epilepsy in children (reviewed in (Sauer et al., 2022b)). Like NaCT, VcINDY is a $Na^+$-driven carboxylate transporter, but VcINDY is primarily a succinate transporter with an electrogenic transport cycle stoichiometry of 3 $Na^+$ ions per succinate (Fig. 1A) (Mulligan et al., 2014; Fitzgerald et al., 2017). Over the past decade, extensive *in vitro* biochemical characterization (Mulligan et al., 2014, 2016; Fitzgerald et al., 2017; Sampson et al., 2020, 2021), and deep structural insight from X-ray crystallography, cryo-electron microscopy

68 (cryo-EM), and computational studies (Mancusso et al., 2012; Mulligan et al., 2016; Nie et al., 2017; Sauer et
69 al., 2021, 2022a), have made VcINDY into the prototypical transporter for understanding the mechanistic details
70 of transport in the DASS family.

71 While the biochemical and structural studies published to-date do not yield a description of the molecular
72 mechanism for the complete VcINDY transport cycle, recent combinations of computational modeling,
73 biochemical, and structural analysis have provided insight (Mulligan et al., 2016; Sauer et al., 2020). Structural
74 studies have revealed VcINDY is a homodimeric membrane protein with two-fold rotational symmetry; however,
75 in all these studies, VcINDY was only observed in a single $C_i$ conformational state in which the substrate binding
76 pockets of both protomers are accessible only from the cytosolic side (*i.e.*, the global homodimer conformation
77 is $C_i$-$C_i$) (Mancusso et al., 2012; Nie et al., 2017; Sauer et al., 2020). Computational and crosslinking studies
78 suggest that VcINDY functions using an elevator mechanism, with a large translocation of the 'transport' domain
79 that carries substrates from one side of the membrane to the other, and a relatively stationary 'scaffold' domain
80 that harbors the dimerization interface (Mulligan et al., 2016). This model is supported by recent structural work
81 revealing a $C_o$ state for LaINDY, a close homolog from *Lactobacillus acidophilus* (Sauer et al., 2020). While these
82 lines of evidence support an elevator mechanism, there has been no experimental observation of a transition
83 between these $C_o$ and $C_i$ states, nor any direct evidence that they are actually responsible for achieving
84 alternating access during transport. Comprehensive validation of this model requires confirming the proposed
85 elevator motions, connecting them to the transport cycle, and understanding how those conformational dynamics
86 enable VcINDY to achieve tight co-substrate coupling between $Na^+$ and succinate to minimize energetically costly
87 slippage of substrates across the membrane (Fig. 1B).

88 In this work, using single-molecule fluorescence resonance energy transfer (smFRET) microscopy, we
89 aimed to directly observe the global conformational dynamics of homodimeric VcINDY in a lipid-bilayer
90 membrane, allowing us to characterize the structural and kinetic details of its transport cycle. To achieve this,
91 we designed two complementary VcINDY constructs for smFRET experiments. Each smFRET construct
92 contained a FRET donor- and acceptor fluorophore pair engineered at residue positions such that the resulting
93 donor-acceptor distance-dependent FRET efficiency ($E_{FRET}$) would report on the conformational dynamics
94 responsible for substrate translocation (Fig. 1C). These smFRET constructs can therefore be used to directly
95 observe the motions that VcINDY undergoes to achieve alternating access (Fig. 1B). In performing smFRET
96 experiments with these constructs, we obtained direct experimental evidence that (i) global conformational
97 dynamics of VcINDY during the transport cycle are consistent with the elevator model of transport, (ii) the
98 individual protomers of homodimeric VcINDY exhibit minimal cooperativity, and (iii) VcINDY minimizes slippage
99 using a mechanism in which co-substrate binding is highly cooperative. These findings provide the first
100 comprehensive description of the molecular underpinnings of the VcINDY transport cycle, and, by extension,
101 deep insight into the transport cycle of all DASS transporters.

102 # Results

103 **smFRET constructs designed to report on substrate translocation**

104 In order to directly monitor the VcINDY conformational dynamics relevant to the transport cycle (Fig. 1B), we
105 designed two smFRET constructs based on the assumption that substrate translocation in VcINDY involves a
106 large-scale conformational change between the $C_o$-$C_o$ and the $C_i$-$C_i$ conformations (*c.f.*, Fig. 1C) (Mancusso et
107 al., 2012; Mulligan et al., 2016; Nie et al., 2017; Sauer et al., 2020). One construct was designed to contain a
108 FRET donor- and acceptor fluorophore pair on the external, periplasmic face of the transport domains of VcINDY
109 whereas the other construct was designed to contain them on the internal, cytosolic face. These complementary
110 designs comprise a 'multi-perspective' approach with an internal self-consistency where any global
111 conformational motions of the VcINDY homodimer occurring during the transport cycle (*e.g.*, an elevator motion)
112 can be detected on both the external and internal sides of the protein.

113 To design these 'external' and 'internal' smFRET constructs, we identified solvent-exposed residues in
114 the transport domain with optimal distances between the two equivalent positions across the homodimer (Fig.
115 1C). Specifically, residues were chosen such that the distance would undergo a significant change upon a
116 transition between the structurally defined $C_i$-$C_i$ and the computationally predicted $C_o$-$C_o$ states (Mancusso et al.,
117 2012; Mulligan et al., 2016; Nie et al., 2017; Sauer et al., 2020). In an optimized smFRET experiment, the
118 corresponding change in the distance-dependent $E_{FRET}$ will utilize the full dynamic range of $E_{FRET}$ from zero to
119 one. To achieve this, we sought residues that moved from separations of less than the Förster distance ($R_0$),
120 which corresponds to the half-maximum $E_{FRET}$ of the donor-acceptor pair, to more than the $R_0$, or vice versa. We
121 used Alexa Fluor 555 as our donor and Alexa Fluor 647 as our acceptor with $R_0$ ~51 Å (Lambert, 2019). Given
122 these considerations, we chose Gly211, located on the extracellular face of the transport domain as our external
123 site, with a predicted $E_{FRET}$ change from ~0.20 to ~0.93 upon a transition from the $C_o$-$C_o$ to the $C_i$-$C_i$ state (Fig.
124 1C). Likewise, we chose Ser436, located on the cytoplasmic face of the transport domain as our internal site,
125 with a predicted $E_{FRET}$ change from ~0.70 and ~0.12 upon transition from the $C_o$-$C_o$ to the $C_i$-$C_i$ state. Single
126 VcINDY homodimer $E_{FRET}$ *versus* time trajectories (*i.e.*, $E_{FRET}$ trajectories) recorded using the external and
127 internal smFRET constructs should then report upon the same set of global VcINDY conformational dynamics
128 involved in substrate translocation but from different perspectives.

129 Biochemically active variants of the two VcINDY smFRET constructs designed above were created,
130 overexpressed, purified, and labeled with donor and acceptor fluorophores to generate the externally and
131 internally labeled smFRET constructs ($VcINDY^{ext}$ and $VcINDY^{int}$, respectively) (see Methods and Materials for
132 extended details) (Fig. 1–Figure Supplement 1). Both $VcINDY^{ext}$ and $VcINDY^{int}$ were able to catalyze substrate
133 translocation in liposomes, and exhibited transport activities that were only three-fold reduced relative to wildtype
134 VcINDY and were similar to the activity of the unlabeled cysteine-containing mutants (Fig. 1–Figure Supplement
135 2). To investigate the conformational dynamics of VcINDY in a membrane, we reconstituted $VcINDY^{ext}$ and
136 $VcINDY^{int}$ into lipid bilayer nanodiscs (Fig. 2) (Denisov and Sligar, 2017). Nanodisc-based experimental

137 conditions are ideal for interrogating the $C_o$ to $C_i$ transition at equilibrium, since both sides of the membrane are
138 exposed to identical solutions. Furthermore, the nanodiscs used here have a diameter of ~108 Å (Bayburt and
139 Sligar, 2010), which helped establish single-molecule resolution by ensuring that only a single VcINDY dimer
140 could occupy each nanodisc. After chromatographic purification, these nanodiscs appeared well dispersed when
141 imaged using negative stain electron microscopy (Fig. 2—Figure Supplement 1).

142 smFRET experiments were performed using a widefield, TIRF microscope to record the fluorescence
143 intensity emitted from individual, immobilized VcINDY-containing nanodiscs (Fig. 2). The corresponding $E_{FRET}$
144 trajectory for each molecule was then calculated using $E_{FRET} = I_{acceptor} / (I_{donor} + I_{acceptor})$, where $I_x$ is the observed
145 intensity of either the donor or the acceptor fluorophore. Along with the chromatographic purification used in
146 nanodisc reconstitution, the selection criteria for $E_{FRET}$ trajectory (see Methods and Materials), ensured that each
147 $E_{FRET}$ trajectory originated from a single VcINDY dimer (Fig. 1—Figure Supplement 1).

148 **Multiple $E_{FRET}$ states are stochastically sampled during VcINDY substrate translocation**

149 To characterize the conformational dynamics of VcINDY during the transport cycle (Fig. 1B), we performed
150 equilibrium smFRET experiments using $VcINDY^{ext}$ or $VcINDY^{int}$ in which the buffer contained saturating
151 concentrations of both $Na^+$ and succinate co-substrates (Buffer HS: High $Na^+$ with Succinate). The
152 conformational dynamics that occur under these conditions are the same as those involved in vectorial
153 transport—even in the absence of a chemical free energy driving force. Thus, by saturating the VcINDY smFRET
154 constructs with both co-substrates, we expected to record $E_{FRET}$ trajectories that report on the equilibrium
155 conformational dynamics of the substrate translocation reaction between a substrate-bound $C_o$ state and a
156 substrate-bound $C_i$ state ($C_o$'' and $C_i$'' in Figure 1B), which we hypothesized resemble the $C_o$-$C_o$ and $C_i$-$C_i$
157 conformations, respectively (Fig. 1C).

158 In the presence of both $Na^+$ and succinate, the $E_{FRET}$ trajectories originating from individual $VcINDY^{ext}$ or
159 $VcINDY^{int}$ dimers stochastically exhibited instantaneous jumps between transiently stable states characterized
160 by distinct $E_{FRET}$ values (*i.e.*, $E_{FRET}$ states) (Fig. 3). Qualitatively, the lifetimes of these $E_{FRET}$ states were generally
161 several seconds, and jumps occurred to $E_{FRET}$ states with both higher and lower average $E_{FRET}$ values. By
162 inspection, it was not uncommon for individual $E_{FRET}$ trajectories to visit many distinct $E_{FRET}$ states (*e.g.*, Fig. 3,
163 lower panels), and the same $E_{FRET}$ states were often revisited within a single $E_{FRET}$ trajectory. Most $E_{FRET}$
164 trajectories, however, exhibited just a few jumps to a low number of distinct $E_{FRET}$ states before relatively rapid
165 photobleaching of the donor and/or acceptor fluorophores prematurely ended our ability to measure $E_{FRET}$.

166 Strikingly, the distribution of $E_{FRET}$ states across the entire population of $VcINDY^{ext}$ or $VcINDY^{int}$ $E_{FRET}$
167 trajectories spanned nearly the entire range of possible $E_{FRET}$ values, from zero to one, and did not exhibit well-
168 defined peaks (Fig. 4). Relative to the signal-to-background ratio of individual $E_{FRET}$ trajectories (Fig. 3), the broad
169 spread of these $E_{FRET}$ state distributions (Fig. 4) suggests that VcINDY dimers exhibit significant conformational
170 heterogeneity. Regardless, the spread of the $E_{FRET}$ state distributions is consistent with the amplitude of

171 fluctuations predicted for a large, elevator conformational transition between the $C_o$-$C_o$ and $C_i$-$C_i$ conformations
172 using the donor-acceptor pairs engineered into both VcINDY$^{ext}$ and VcINDY$^{int}$ (Fig. 1C).

173 **VcINDY samples $C_o$-$C_o$, $C_i$-$C_i$, and mixed $C_o$-$C_i$ conformational states during substrate transport**

174 After observing dynamic $E_{FRET}$ trajectories that exhibited instantaneous jumps between widely distributed $E_{FRET}$
175 states for both VcINDY$^{ext}$ and VcINDY$^{int}$ (Figs. 3 and 4), we desired to understand how these $E_{FRET}$ states and
176 dynamics correspond to the underlying conformational states and dynamics of the VcINDY transport cycle (Fig.
177 1B). To do so, we sought the simplest, quantitative description of the $E_{FRET}$ trajectories that was globally
178 consistent with all the $E_{FRET}$ trajectories recorded in an experiment. Because of the instantaneous jumping
179 behavior of the $E_{FRET}$ trajectories (Fig. 3), we used a global hidden Markov model (HMM) to quantify the common
180 $E_{FRET}$ states and kinetics present in all the $E_{FRET}$ trajectories (see Methods and Materials for details) (Fig. 4–
181 Figure Supplements 1-2). In the presence of both co-substrates, we found that the most parsimonious global
182 HMMs that could account for the observed complexity in the $E_{FRET}$ trajectories had three $E_{FRET}$ states for both
183 VcINDY$^{ext}$ and VcINDY$^{int}$ (Fig. 4, Fig. 4–Figure Supplements 3-4). Given that we find three $E_{FRET}$ states in buffer
184 HS from both smFRET perspectives, and that the $E_{FRET}$ trajectories recorded under different $Na^+$ and succinate
185 conditions were also best described by three $E_{FRET}$ states (see below) (Fig. 4—Figure Supplement 3), we
186 concluded that our smFRET data report primarily on transitions between three common, global conformations of
187 the VcINDY dimer.

188 According to the alternating access principle, at least some part of these three $E_{FRET}$ states should
189 correspond to the $C_o$ and $C_i$ states in the transport cycle (Jardetzky, 1966) (Fig. 1B). For VcINDY$^{ext}$, the $E_{FRET}$ =
190 0.25 state is consistent with our estimate of $E_{FRET}$ = 0.20 for the $C_o$-$C_o$ conformation, and the $E_{FRET}$ = 0.85 state
191 is consistent with our estimate of $E_{FRET}$ = 0.93 for the $C_i$-$C_i$ conformation (Fig. 1C, Fig. 4–Figure Supplement 4).
192 Likewise, for VcINDY$^{int}$, the $E_{FRET}$ = 0.83 state is consistent with our estimate of $E_{FRET}$ = 0.70 for the $C_o$-$C_o$
193 conformation, and the $E_{FRET}$ = 0.16 state is consistent with our estimate of $E_{FRET}$ = 0.12 for the $C_i$-$C_i$ conformation
194 (Fig. 1C, Fig. 4–Figure Supplement 4). Thus, the $E_{FRET}$ states we observe in our smFRET experiments are
195 broadly consistent with the elevator mechanism suggested by previous structural work and illustrate how these
196 large-scale conformational changes are coupled to substrate transport.

197 The small differences between the expected and observed $E_{FRET}$ values ($\Delta E_{FRET} \sim 0.1$) might be due to:
198 (i) differences in the $C_o$-$C_o$ and/or $C_i$-$C_i$ structures which nanodisc-embedded VcINDY adopts in our smFRET
199 experiments and between those in the computational, X-ray, and cryo-EM studies (Mancusso et al., 2012;
200 Mulligan et al., 2016; Nie et al., 2017; Sauer et al., 2020), (ii) structural perturbations of VcINDY due to
201 fluorophore labeling, (iii) linker contributions to the distance between fluorophores, (iv) constraints on fluorophore
202 mobility due to interactions with protein and/or membrane, or even (iv) photophysical complications, such as
203 'photoblinking', that effect $E_{FRET}$ estimates. Given the experimental consistency with the structural estimates for
204 both VcINDY$^{ext}$ and VcINDY$^{int}$, we assigned the $E_{FRET}$ states discussed above to the $C_o$-$C_o$ and $C_i$-$C_i$

205 conformational states. Additionally, these assignments are self-consistent with respect to the equilibrium state
206 population distribution of the transport cycle (Fig. 1) in that the most occupied $E_{FRET}$ state in both smFRET
207 experiments was the $C_i$-$C_i$ VcINDY conformational state and was thus independent of the smFRET perspective
208 used (Fig. 4).

209 The remaining, unassigned $E_{FRET}$ state can be explained as either a 'mixed' $C_o$-$C_i$ conformation of the
210 VcINDY dimer or a new, 'intermediate' conformation distinct from $C_o$-$C_o$ and $C_i$-$C_i$. Based on biochemical and
211 structural considerations, we favor assigning this $E_{FRET}$ state to the more parsimonious, mixed conformation. The
212 existence of such a mixed conformation is only possible if the protomers of VcINDY operate independently,
213 which is suggested by previous Hill coefficient measurements for succinate transport (Mulligan et al., 2014).
214 Additionally, the two-fold rotational symmetry of the VcINDY dimer renders the $C_o$-$C_i$ and $C_i$-$C_o$ conformations
215 structurally degenerate, and thus the $C_o$-$C_i$ and $C_i$-$C_o$ $E_{FRET}$ states would both yield the same $E_{FRET}$ value, which
216 is consistent with our analysis. In contrast, similar symmetry considerations for a VcINDY dimer with a unique
217 intermediate protomer conformation would yield up to six distinct $E_{FRET}$ states in the absence of strict protomer
218 cooperativity or anti-cooperativity. Finally, computational alignment of the VcINDY scaffold domain of the $C_o$-$C_o$
219 and $C_i$-$C_i$ conformations shows that the donor and acceptor fluorophores in a mixed $C_o$-$C_i$ state would be ~50 Å
220 apart for $VcINDY^{ext}$ and ~59 Å apart for $VcINDY^{int}$—distances that correspond to $E_{FRET}$ values of 0.53 and 0.29,
221 respectively. Given the caveats described above, these estimates are in reasonable agreement with the $E_{FRET}$
222 values of 0.54 and 0.42 that we obtained from our global HMM analysis of the smFRET data (Fig. 4–Figure
223 Supplement 4).

224 Despite the limited observation window of any one individual $E_{FRET}$ trajectory, the global HMM analyses
225 we performed provide a quantification of the kinetics present within the collective set of $E_{FRET}$ trajectories (Fig.
226 4—Figure Supplement 4). Regardless of the smFRET perspective used ($VcINDY^{ext}$ or $VcINDY^{int}$), the elevator
227 motion of a single protomer in the VcINDY dimer across the membrane occurs in these experiments at a rate of
228 ~0.4 $s^{-1}$ (*i.e.*, once every ~2.5 seconds), with no apparent directional dependence. Notably, direct transitions
229 between $C_o$-$C_o$ and $C_i$-$C_i$ where both protomers undergo an apparently simultaneous transition within the
230 temporal resolution of our TIRF microscope were approximately an order of magnitude slower (~0.04 $s^{-1}$), and
231 therefore much less likely to occur. This suggests that the individual protomers of a VcINDY dimer primarily
232 undergo the translocation reaction in an independent and uncoordinated manner. Overall, the elevator motions
233 of VcINDY responsible for substrate translocation that occur in these experiments are approximately an order of
234 magnitude faster than the turn-over rate for transport measured in bulk biochemical transport experiments of
235 ~0.02 $s^{-1}$ (Mulligan et al., 2014). Along with the fact that our smFRET experiments were performed at lower a
236 temperature (21 °C *versus* 30 °C), this suggests that VcINDY undergoes multiple substrate translocation
237 reactions before a productive transport event occurs, and that the rate limiting step of VcINDY, and possibly
238 DASS family, catalyzed transport may involve substrate binding and/or dissociation.

239 **VcINDY exhibits conformational dynamics that are largely substrate independent**

240 The basic mechanistic model of a transport cycle for VcINDY makes several fundamental predictions regarding
241 the conformational dynamics that occur during transport (Fig. 1B). Consistent with the alternating access
242 hypothesis (Jardetzky, 1966), VcINDY should be able to switch from a $C_o$ to a $C_i$ conformation in the apo,
243 substrate-free state. Also, to preserve substrate coupling, we expect that the partially bound transporter ($C_o$' and
244 $C_i$' in Fig. 5) will not undergo outward to inward transitions (and vice versa) to minimize uncoupled slippage of
245 $Na^+$ or succinate. To test these predictions, we performed additional smFRET experiments using $VcINDY^{int}$ in
246 the absence of both co-substrates (*i.e.*, in the apo state) (Buffer LX: Low $Na^+$ with no succinate) as well as in the
247 presence of high concentrations of one co-substrate but the absence of the other (*i.e.*, in the only bound $Na^+$- or
248 only succinate bound states) (Buffer HX: High $Na^+$ with no succinate; Buffer LS: Low $Na^+$ with Succinate).
249 Because of the consistency between $VcINDY^{int}$ and $VcINDY^{ext}$ we observed in buffer HS (Figs. 3,4), these
250 substrate-dependence experiments were done with only the $VcINDY^{int}$ construct. Where appropriate, we
251 replaced $Na^+$ with choline to maintain ionic strength and osmolarity. We note that all of our buffers likely contain
252 trace (*i.e.*, 'low') amounts of contaminating $Na^+$, but at several orders of magnitude less than the measured
253 Michaelis constant, $K_M$ = 41.7 mM, for transport (Mulligan et al., 2014).

254 As observed for the smFRET experiments recorded in the presence of high concentrations of both co-
255 substrates (Buffer HS), the smFRET experiments recorded under all three additional co-substrate conditions
256 (Buffers LX, HX, and LS) yielded $E_{FRET}$ trajectories that spontaneously exhibited instantaneous jumps between
257 $E_{FRET}$ states spanning a comparably wide range as was seen in buffer HS (Fig. 4). When we analyzed these data
258 using the same global HMM approach described above, the most parsimonious quantification of the sets of $E_{FRET}$
259 trajectories in each smFRET experiment was again a global HMM with three $E_{FRET}$ states (Fig. 4–Figure
260 Supplement 3). In these global HMMs, both the $E_{FRET}$ states and rate constants for the transitions between them
261 were very similar to those obtained in Buffer HS (Fig. 4–Figure Supplement 4). While there were slight differences
262 in the equilibrium population distribution of the three $E_{FRET}$ states observed in each co-substrate condition, the
263 kinetics of these global HMMs were relatively unchanged with single protomer translocation reactions occurring
264 all at approximately the same rate of ~0.5 $s^{-1}$. Thus, our quantitative kinetic analysis reveals that the
265 conformational motions of VcINDY that are probed along the coordinate between the donor and acceptor
266 fluorophore in $VcINDY^{int}$ are relatively independent of the co-substrate composition. Although these results
267 conform to our expectation for the apo state, the observation of frequent transitions in the $E_{FRET}$ trajectories
268 recorded under the single-substrate conditions was unexpected.

269 **Thermodynamic modeling shows that compensatory tuning of co-substrate binding and dissociation**
270 **can minimize slippage cycles**

271 In search of an explanation for the surprising kinetics observed under the single-substrate conditions, we next
272 analyzed the thermodynamic efficiency of the VcINDY transport cycle. We modeled the free-energy transduction

273 of a secondary active transporter using Hill's method of cycles (Hill, 2005) to determine how the different
274 molecular processes involved in transport might contribute to slippage. For simplicity, we considered co-
275 substrate binding as a strictly sequential, two-step process with mirror symmetry (*i.e.*, the same binding/release
276 order on both faces of the membrane). To be concrete, we considered the most parsimonious molecular
277 interpretation of this kinetic scheme for secondary active transport where (i) the rate constants are all first-order
278 or pseudo-first order, (ii) the rate constants are independent of the $C_o$ or $C_i$ state, and (iii) the translocation
279 reaction is independent of substrate binding status (Fig. 5). The resulting, simplified kinetic scheme has three
280 Hill cycles—two of which are involved in slippage (cycles *a* and *b*) and one that is responsible for transport (cycle
281 *c*) (Fig. 5).

282 We then calculated the thermodynamic efficiency, $\eta$, of a transporter with these assumptions (Fig. 5) (Hill,
283 2005). For a maximally efficient transporter, $\eta \approx 1$ and the transporter tightly couples free energy from the driving
284 to the driven co-substrate with very little slippage. In that situation, the thermodynamic efficiency is $\eta \propto 1 -$
285 $(\eta_{ac} - \eta_{bc}) + \cdots$ with small higher order terms; here we have assumed $A$ is the driving substrate, but the
286 conclusions discussed below are independent of this. Under our assumptions,

287 $$\eta_{ac} = \frac{J_a}{J_c} = \left(\frac{[A]_o^m - [A]_i^m}{[A]_o^m[B]_o^n - [A]_i^m[B]_i^n}\right)\left(\frac{2k_t + k_d''}{k_a''}\right),$$

288 and

289 $$\eta_{bc} = \frac{J_b}{J_c} = \left(\frac{[B]_o^n - [B]_i^n}{[A]_o^m[B]_o^n - [A]_i^m[B]_i^n}\right)\left(\frac{k_t([A]_o^m + [A]_i^m) + k_a'[A]_o^m[A]_i^m}{k_d'}\right),$$

290 where $J_\kappa$ is the cycle flux for cycle κ, concentrations are indicated by square brackets, $A$ and $B$ are the first and
291 second binding co-substrates with stoichiometries $m$ and $n$, respectively, the translocation rate constant is $k_t$,
292 association and dissociation rate constants are $k_a$ and $k_d$, respectively, and prime and double-prime denote the
293 first and second binding reactions, respectively (Fig. 5). The first terms in these equations show that the relative
294 amount of slippage that a transporter undergoes depends on the instantaneous thermodynamic driving forces
295 *via* the co-substrate chemical gradients, while the second terms show that it also depends on the translocation
296 and substrate binding and dissociation reaction kinetics. Thus, the only reliable way nature can optimize this
297 transporter into a highly efficient free energy transducer over a broad range of environmental conditions is to
298 have evolved control over slippage *via* evolutionary tuning of these rate constants to reduce the total magnitude
299 of $\eta_{ac}$ and $\eta_{bc}$. This suggests that optimal transporters have faced evolutionary pressure to decrease $k_t$, $k_a'$
300 and/or $k_d''$, and to increase $k_a''$ and/or $k_d'$ such that the first binding co-substrate weakly binds until the second
301 arrives and then both co-substrates can tightly bind. Unfortunately, tuning these rate constants will also affect
302 the overall transport cycle flux, $J_c$, and this creates a speed-accuracy tradeoff.

303 The speed-accuracy tradeoff can, however, be navigated. On the molecular level, the clearest way to
304 reduce slippage is for the binding pocket to stabilize the *apo* and fully bound states (C and C"), by some amount
305 $\Delta G'$ and $\Delta G''$, respectively, and to source all of that energy from a compensatory destabilization of the partially

306 bound conformation, C', by an amount $\Delta G' + \Delta G''$, all without affecting the transition state energy barriers (Fig.
307 6). This is a conceptually similar idea to the use of substrate binding energy to stabilize the transition state for
308 enzyme-substrate transition state complementarity (Fersht, 2017). In our case, this isoenergetic change
309 increases $k_a'$ and $k_d''$ while decreasing $k_a''$ and $k_d'$, which reduces slippage and increases the thermodynamic
310 efficiency of the transporter. It also has the effect of increasing the transport cycle flux *via* ~75% of the terms
311 defining $J_c$ (see *Methods and Materials* for the expression for $J_c$). Given this substantial ability to speed up
312 transport in the complicated expression for $J_c$, we suspect that these compensatory, isoenergetic binding and
313 dissociation reaction tunings optimally navigate the speed-accuracy tradeoff by simultaneously decreasing the
314 relative fraction of slippage while increasing the total amount of transport. The exact extent of these abilities,
315 however, depends on the instantaneous internal and external co-substrate concentrations, which can vary
316 significantly across physiologically relevant conditions (Fig. 6–Figure Supplement 1) (Lo et al., 2006).
317 Regardless, this thermodynamic modeling of the free energy transduction efficiency of a secondary active
318 transporter predicts that slippage can be reduced simply by isoenergetic optimization of the energy landscape
319 of the co-substrate binding reaction (Fig. 6). In other words, increased cooperativity of co-substrate binding can
320 itself lead to minimized slippage.

321 Finally, we also used this thermodynamic modeling-based approach to estimate the occupancy of apo
322 VcINDY in our smFRET experiments performed in presence of only saturating $Na^+$ (Buffer HX). Specifically, we
323 modeled the reported $K_M$ and $V_{max}$ values for the $Na^+$ titration and succinate titration experiments that recorded
324 succinate uptake rates in the biochemical proteoliposome-based transport assay data of Mulligan and coworkers
325 (see *Methods and Materials* for extended details) (Mulligan et al., 2014). This was an underdetermined problem,
326 so we assumed that a single, average rate constant defined several molecular processes: $\langle k \rangle \equiv k_t = k_d' = k_d''$.
327 Markov chain Monte Carlo optimization yielded estimates of $k_a' = 1.5 \times 10^7 M^{-3} s^{-1}$, $k_a'' = 7.0 \times 10^8\ M^{-1} s^{-1}$, and
328 $\langle k \rangle = 1.05 \times 10^3\ s^{-1}$ (Fig. 5-Figure Supplement 1 and 2), and reasonably matched the original titration data (Fig.
329 5-Figure Supplement 3). The mismatch is due to the common rate constant assumption, and probably to
330 differences in the actual binding mechanism assumed here (*e.g.*, perhaps not all three $Na^+$ ions bind before
331 succinate). Regardless, these estimates are consistent with the biochemical transport data in the context of our
332 kinetic mechanism, so we used them to calculate the steady-state probability of apo VcINDY in Buffer HX to be
333 6.5% (see *Methods and Materials*). This estimate suggests that even with 100 mM $Na^+$ in solution, VcINDY still
334 spends a non-negligible portion of time with an unoccupied binding pocket. In this light, the majority of the
335 unexpected elevator motions present in the $E_{FRET}$ trajectories recorded in the presence of only one co-substrate
336 might originate from apo, rather than partially bound, VcINDY.

337 **Dicarboxylate substrate binding pocket is enthalpically stabilized by sodium ions**

338 To obtain atomic-resolution insight into the $Na^+$ and dicarboxylate substrate binding reaction for the VcINDY
339 transport cycle, we determined how the conformational state of the VcINDY homodimer is influenced by different

340 dicarboxylate substrates. We therefore separately crystallized detergent-solubilized VcINDY with $Na^+$ and three
341 different $C_4$-dicarboxylate substrates (succinate, fumarate, and malate) and solved their structures at 3.09 Å,
342 3.29 Å, and 3.50 Å, respectively. Regardless of the dicarboxylate substrate identity, VcINDY adopted the same
343 $C_i$-$C_i$ state in all three of these structures. Similarly, as seen in the previous structure of the $C_i$-$C_i$ state (Mancusso
344 et al., 2012; Nie et al., 2017; Sauer et al., 2020), the binding pocket of the dicarboxylate substrate in all three
345 structures was partially comprised of two hairpin loops that coordinated distinct $Na^+$ ions, Na1 and Na2 (Fig. 7).
346 Given this binding geometry, it is possible that tight binding of both co-substrates requires stabilization of these
347 hairpin loops and that their local conformational rearrangements gates binding and/or release of the co-
348 substrates.

# 349 Discussion

350 **The VcINDY transport domain undergoes elevator motions to enable alternating access**

351 The ubiquitous presence in our experiments of stochastic, instantaneous transitions between $E_{FRET}$ states
352 consistent with the $C_o$-$C_o$ and the $C_i$-$C_i$ conformations is the first direct evidence for the hypothesis that VcINDY
353 uses an elevator transport mechanism to enable alternating access (Fig. 3) (Mulligan et al., 2016). Because we
354 directly observed these stochastic, elevator motions in the presence of substrates but absence of an
355 electrochemical gradient (Buffer HS) and also in the absence of any co-substrates at all (Buffer LX), it is clear
356 that the VcINDY transport domain can translocate the substrate binding site across the membrane using only
357 thermal energy—as is expected for the conformational motions of a secondary active transporter that are
358 responsible for transport. Moreover, the rate constants for that process are on the order of $10^{-1}$ $s^{-1}$ (Fig. 4–Figure
359 Supplement 4), suggesting that the energy barrier separating the $C_o$ and $C_i$ state along the translocation reaction
360 coordinate is not prohibitively high. Since the VcINDY transport cycle is much slower and occurs with a rate on
361 the order of $10^{-2}$ $s^{-1}$ (Mulligan et al., 2014), it seems that multiple back and forth substrate translocation events
362 occur before a productive transport event is completed. This observation is consistent with a model in which a
363 molecular process other than transport domain translocation govern the transport rate (*e.g.*, gating dynamics
364 within the substrate binding pocket itself).

365 **The conformational dynamics of VcINDY protomers are non-cooperative**

366 The experimental observation of a mixed $C_o$-$C_i$ conformation for the VcINDY dimer constrains the role that the
367 two protomers can play in the transport cycle. Previously, proteoliposome-based transport experiments
368 determined that VcINDY transports succinate with a Hill coefficient of 0.88 ± 0.13 (Mulligan et al., 2014). Given
369 the VcINDY transport stoichiometry of 3:1 $Na^+$:dicarboxylate (Fitzgerald et al., 2017), this Hill coefficient
370 measurement suggested that the VcINDY transport cycle is non-cooperative and that each VcINDY protomer
371 can independently transport succinate. We supported this biochemical hypothesis on a molecular level by
372 interpreting our experimental observation of the $E_{FRET}$ state assigned to the mixed $C_o$-$C_i$ conformation as direct

373 evidence that the VcINDY protomers undergo non-cooperative substrate translocation reactions during vectorial
374 transport. Since the VcINDY dimer can significantly occupy the $C_o$-$C_i$ state, the two VcINDY protomers must not
375 undergo a strictly cooperative translocation reaction (*i.e.*, $C_o$-$C_o \rightleftharpoons C_i$-$C_i$). Furthermore, they must not undergo a
376 strictly anti-cooperative translocation reaction either (*i.e.*, $C_o$-$C_i \rightleftharpoons C_i$-$C_o$), because this behavior would preclude
377 the occupation of the $C_o$-$C_o$ and $C_i$-$C_i$ conformations that we observe in our smFRET experiments and in
378 structural studies. Therefore, our results provide direct evidence that the VcINDY protomers undergo non-
379 cooperative translocation reactions, and that the VcINDY transport cycle itself can be considered to occur
380 independently in each protomer.

381 In support of this idea, a recent structure of CitS, another homodimeric elevator transporter in a different
382 structural family, reveals a CitS dimer with one inward-facing and one outward-facing protomer (Kim et al., 2017),
383 and a recent high-speed atomic force microscopy study of the CitS elevator translocation motion reported that
384 CitS undergoes non-cooperative interprotomer conformational dynamics (Maity et al., 2022). Combined with
385 evidence that $Glt_{Ph}$, an elevator-type, glutamate transporter that unlike VcINDY is from a thermophilic organism,
386 also shows independence between the motions of its three protomers (Akyuz et al., 2013; Erkens et al., 2013;
387 Ruan et al., 2017), these results suggest that such independence may be a general feature of oligomeric elevator
388 transporters (Garaeva and Slotboom, 2020).

389 **Slippage cycles are avoided without inhibiting VcINDY transport domain translocation**

390 To avoid wasting the free energy provided by the $Na^+$ gradient that drives transport of substrates across the
391 membrane, the conformational motions of VcINDY must be coordinated. In particular, VcINDY must minimize
392 slippage cycles in which $Na^+$ ions are transported across the membrane independent of dicarboxylate (Fig. 1).
393 We had hypothesized that VcINDY avoids such slippage cycles by inhibiting the substrate binding pocket
394 translocation reaction (*i.e.*, $C_o \rightleftharpoons C_i$) when sub-stoichiometric amounts of the co-substates are bound, and by
395 promoting those motions only when VcINDY is either empty or fully bound. However, the smFRET experiments
396 we recorded under single substrate conditions, yielded $E_{FRET}$ trajectories that exhibited no discernable
397 differences in the $E_{FRET}$ states or their rates of transitions, regardless of the presence of relatively high
398 concentrations of either individual co-substrate in solution (Fig. 4–Figure Supplement 4). Given our determination
399 that those observed transitions could reasonably correspond to apo VcINDY, it is quite possible that transitions
400 between $C_o$ and $C_i$ in partially bound states are directly suppressed and that we were not able to observe those
401 effects, but our smFRET experiments suggest that VcINDY also uses another, additional mechanism to minimize
402 slippage (Fig. 1B).

403 There are at least two additional mechanisms that VcINDY can use to minimize slippage. One possibility
404 is a secondary conformational change—independent of $C_o \rightleftharpoons C_i$ translocation—to 'gate' both binding and release
405 of co-substrates. For instance, while VcINDY could be able to translocate substrates across the membrane if the
406 $C_o \rightleftharpoons C_i$ transition is not completely inhibited, a slippage cycle cannot be completed without co-substrate release.

407 Mechanistically, such gating could be achieved with an additional VcINDY conformational equilibrium that is
408 relatively independent of the transport domain translocation reaction $C_o \rightleftharpoons C_i$. Without direct structural insight
409 into such a hypothetical equilibrium, it is attractive to think that it might involve a conformational rearrangement
410 of the binding pocket and, in particular, the hairpin loops (*c.f.*, Fig. 7). In this scenario, the transitions we observe
411 in the smFRET data for partially bound VcINDY would reflect transitions between so-called "occluded" states.

412 Another possible mechanism to minimize slippage is to ensure that co-substrate binding is extremely
413 cooperative, such that stable binding requires both co-substrates to be present. In our smFRET experiments
414 performed in Buffers HX and LS, this mechanism would manifest as transitions in the $E_{FRET}$ trajectories that
415 predominately correspond to transport domain translocation of apo VcINDY. This alternative scenario is
416 consistent with the non-negligible fraction of apo VcINDY we estimated to be present under these experimental
417 conditions. Furthermore, it could explain the apparent lack of substrate dependence observed relative to our
418 smFRET experiments in Buffer LX (Fig. 4-Figure Supplement 4). This cooperative co-substrate binding scenario
419 agrees with our thermodynamic modeling (Fig. 5), which predicts that an optimized transporter that has evolved
420 to minimize slippage cycle flux should have extremely stable apo and fully bound states with very weak binding
421 of the initial co-substrate(s) (Fig. 6). The extent of that optimization reflects how nature has navigated the speed-
422 accuracy tradeoff between rapid transport and minimal slippage. This raises the possibility that some secondary
423 active transporters undergo a non-negligible amount of slippage in order to be efficient at transporting the driven
424 co-substrate as long as they do not significantly waste the free energy of the driving co-substrate.

425 Experimental evidence is also consistent with a cooperative co-substrate binding mechanism. For
426 instance, our X-ray crystallographic structures show that Na1, Na2, and dicarboxylate substrates all interact with
427 common hairpin loop elements (Fig. 7). That the VcINDY conformation is effectively independent of dicarboxylate
428 identity suggests that this fully bound conformation is very stable—as predicted in our modeling of optimal co-
429 substrate binding. Moreover, recent experiments demonstrated that, in the presence of high concentrations of
430 only $Na^+$, residues associated with the substrate binding pocket are protected from PEG modification (Sampson
431 et al., 2020; Sauer et al., 2022a) indicating some interaction between $Na^+$ and the apo VcINDY binding pocket.
432 This result is consistent with a $Na^+$-first binding order, and with predictions that slippage is minimized and that
433 transport is optimized by weak binding of the first co-substrate(s) (Fig. 6). In future work, determination of the
434 affinities and binding order of co-substrates, together with structure characterization of the sites, will be required
435 to develop a comprehensive understanding of how co-substrate binding is employed as a mechanism to avoid
436 slippage cycles during vectorial transport by VcINDY.

## 437 Conclusion

438 Previous studies of the structure, transport biochemistry, and alternating access mechanism of VcINDY have
439 established it as a prototypical membrane-bound transporter of the DASS family (Mancusso et al., 2012; Mulligan
440 et al., 2014, 2016; Nie et al., 2017; Fitzgerald et al., 2017; Sauer et al., 2020; Sampson et al., 2020). Here, we

441 have advanced this fundamental understanding of the DASS family and secondary active transport by directly
442 determining how the conformational dynamics of VcINDY enable it to achieve alternating access, and how those
443 dynamic motions are tuned in order to maintain the efficiency of the transport cycle. Specifically, our study
444 provides direct evidence that (i) the VcINDY translocation reaction uses a thermally driven, elevator mechanism;
445 (ii) VcINDY protomer conformational dynamics are non-cooperative; (iii) the VcINDY transport cycle uses
446 cooperative substrate binding to minimizes slippage; and (iv) cooperative substrate binding is a general approach
447 to optimize transport efficiency for certain secondary active transporters. Altogether, these findings immediately
448 suggest future studies aimed at determining the extent to which highly cooperative co-substrate binding and/or
449 additional conformational dynamics that gate transport (Drew and Boudker, 2016; Lolkema and Slotboom, 2019;
450 Stein and Lieb, 1986) enable VcINDY to avoid slippage cycles during vectorial transport. Overall, the powerful
451 smFRET-based experimental modality for interrogating the function and regulation of VcINDY established here
452 is easily extended to study the transport cycles of other DASS family transporters, and even dimeric transporters
453 from other families, to further our understanding of secondary active transport.

# 454 Methods and Materials

455 **Expression and purification of VcINDY**. Expression and purification of wild type VcINDY was carried out
456 according to our previous protocol (Mancusso et al., 2012). Briefly, *Escherichia coli* (*E. coli*) BL21-AI cells
457 (Invitrogen) were transformed with a modified pET vector encoding N-terminal 10X His tagged VcINDY. Cells
458 were grown for 16 hours post-induction at 19°C. After cell breakage, membranes were solubilized in 1.2% N-
459 decyl-β-maltoside (DM) and the protein was purified on a Ni-NTA affinity column (Qiagen). Following His-tag
460 removal, VcINDY was further purified by size-exclusion chromatography (SEC) in buffer containing 25 mM Tris
461 pH 8, 100 mM NaCl, 5% glycerol, 0.1% DM unless otherwise indicated.

462 **Purification of VcINDY mutants**. Expression and purification of VcINDY mutants G211C and S436C was
463 performed as with the wildtype protein, but with the following modifications. All buffers contained 10 mM sodium
464 citrate but not glycerol. Membranes were solubilized in 1.0% N-dodecyl-β-maltoside (DDM). The protein was
465 eluted from Ni-NTA agarose beads using 300 mM imidazole. Finally, the SEC buffer contained 25 mM Tris pH
466 8, 100 mM NaCl, 0.1% DDM and 0.5 mM TCEP.

467 **Expression, purification and biotinylation of membrane scaffolding protein**. Expression and purification of
468 membrane scaffolding protein (MSP1E3D1) was carried out according to a previously published protocol
469 (Denisov et al., 2004). In brief, *E. coli* BL21-Gold (DE3) cells (Agilent) were transformed with a modified pET 28a
470 vector encoding N-terminal 7X His tagged MSP with a mutated cysteine at position 277 for biotinylation. Cells
471 were grown at 30°C for 4 hrs post 0.1 mM IPTG induction at OD 0.8. After cell breakage, lysate was bound to
472 Ni-NTA agarose beads (Qiagen) for 4 hours with nutation at 4°C. Protein was eluted with 100 – 250 mM imidazole
473 and dialyzed into 100 mM Tris pH 7.4, 300 mM NaCl for 1 hr at 4°C. The His-tag was then removed by overnight

474 TEV digestion at 12°C. Cleaved MSP protein was subsequently biotinylated using EZ-Link Maleimide-PEG11-
475 Biotin (Promega) according to the manufacturer's instructions. Specifically, a 20-fold molar excess of biotin
476 reagent dissolved in DMSO was incubated with protein overnight at 4°C. Labeled MSP1E3D1-T277C protein
477 was further purified by SEC in 100 mM NaCl, 1 mM TCEP, 20 mM Tris pH 7.4.

478 **Fluorophore Labeling.** Stock solutions of Alexa Fluor 555 C2 maleimide (AF555) and Alexa Fluor 647 C2
479 maleimide (AF647) were prepared in anhydrous DMSO at 3mM and stored at -20°C. Prior to labeling, a 1 mg/ml
480 solution of VcINDY (total of 0.5mg to 1mg) was treated with 10mM DTT for 2hrs at 4°C to reduce the cysteines.
481 DTT was then removed by 3 serial dilutions in SEC buffer (25 mM tris pH 8.0, 100 mM NaCl, 5% glycerol, 0.15%
482 DDM, 1 mM TCEP) followed by re-concentration with an Amicon concentrator (cutoff 50 kDa). This preparation
483 was incubated with a 10-fold molar excess of AF555 and AF647 overnight at 4°C, protected from light. The
484 resulting solution was purified on Superdex 200 10/300 GL size exclusion column to remove the unreacted dye.
485 Fractions from the elution peak were combined and the labeling stoichiometry was determined with a
486 spectrophotometer using the following wavelengths and extinction coefficients: VcINDY: $\lambda$=280 nm with $\epsilon$ =
487 57075 $cm^{-1}M^{-1}$; AF555: $\lambda$= 556 nm with $\epsilon$= 155,000 $cm^{-1}M^{-1}$; AF647: $\lambda$= 651 nm with $\epsilon$= 270,000 $cm^{-1}M^{-1}$. Typical
488 labeling efficiency was 42% for each dye.

489 **Nanodisc Reconstitution.** A thin film of *E. coli* polar lipid (EPL) was prepared by adding 10 mg of chloroform
490 stock solution to a glass test tube. The solvent was evaporated with argon gas and the test tube was placed in
491 a vacuum chamber at ~1 mTorr for ~2 hr. This lipid film was resuspended by adding 285 µl of nanodisc buffer
492 (20mM Tris pH7.4; 100mM NaCl, 0.5mM EDTA, 0.5mM TCEP) followed by vortexing and sonication in an
493 ultrasonic bath (Laboratory Supplies Co. Inc, Model G112SP1T) with 10 sec bursts alternating with 10 sec rests
494 for a total of 3min. This aqueous lipid solution was solubilized by adding 215 µl of 10% DDM to produce 500 µl
495 of final lipid stock concentration at 20mg/ml.
496 To reconstitute VcINDY into nanodiscs, detergent-solubilized EPL was added to VcINDY at a molar ratio
497 of 280 and incubated on ice for 10 min. Biotinylated MSP was then added to this mixture at an 8-fold molar
498 excess to produce 500 µl of a solution containing 2.5mM EPL, 72 µM MSP, 9 µM VcINDY and 7.2 mM DDM.
499 This solution was incubated at 4°C for 1hr followed by the addition of SM-2 Bio-Beads in three steps: 300 mg
500 initially, 200 mg added 60 min later, and 100 mg added at 90 min later and incubated overnight. During these
501 incubations, solutions were kept at 4°C and gently stirred.
502 Nanodiscs containing VcINDY were purified by incubating the solution with 0.5 ml of Ni-NTA beads pre-
503 equilibrated with nanodisc buffer (20 mM Tris pH=7.4; 100 mM NaCl; 0.5 mM EDTA; 0.5 mM TCEP) for 30 min
504 at 4°C. The beads were packed into a column and washed with 1 ml of nanodisc buffer. Nanodiscs containing
505 VcINDY were then eluted with 2 ml nanodisc buffer supplemented with 0.3 M imidazole and the peak elution
506 fractions were pooled and concentrated with an Amicon concentrator (cutoff 50 kDa). The concentrated sample
507 was fractionated on Superdex 200 10/300 GL size exclusion column (GE Healthcare) pre-equilibrated and eluted

508 with nanodisc buffer. The fractions were evaluated by SDS-PAGE and those containing both MSP and VcINDY
509 were pooled, and concentrated to ~0.2-0.4 mg/ml. Typical yield for 1mg of VcINDY was ~0.4 mg of reconstituted
510 protein (VcINDY plus MSP). Electron microscopy grids were prepared in 2% (w/v) phosphotungstic acid (pH 7.5)
511 and were examined in a Talos L120C transmission electron microscope (FEI-Thermo Fisher Scientific).
512 Nanodisc samples were frozen in aliquots and stored at –80°C.

513 **Proteoliposome Reconstitution and Transport Assay.** VcINDY was reconstituted into proteoliposomes as
514 previously described (Mulligan et al., 2016, 2014). These proteoliposomes were then used in succinate transport
515 assays as previously described (Mulligan et al., 2016, 2014). Briefly, proteoliposomes were exchanged into
516 external buffer containing tritiated succinate with an inward facing $Na^+$ gradient, samples taken at various time
517 points were quenched and rapidly filtered over a 0.22 $\mu m$ nitrocellulose membrane, and then succinate content
518 inside the proteoliposomes was measured using scintillation counting. Transport rates were calculated from a
519 linear fit to at least three data points within the first minute of the transport reaction.

520 **TIRF Microscopy.** smFRET imaging experiments were performed on a prism-based, wide-field TIRF
521 microscope at a temperature of 21 ± 1 °C. Briefly, a 532 nm diode-pumped solid-state continuous-wave laser
522 (Laser Quantum, GEM532) was directed through an acousto-optic modulator (AOM) (Isomet, IMDD-P80L) such
523 that the +1 order peak is directed toward a prism suspended over a 60x, 1.2 NA water immersion objective
524 (Nikon). VcINDY embedded nanodiscs were tethered to the surface of quartz slides derivatized with dilute biotin-
525 poly(ethylene)-glycol (PEG) in PEG *via* a biotin-streptavidin-biotin bridge, and illuminated with the TIR field
526 generated at the slide/buffer interface. The instantaneous illumination power incident at the prism entry face was
527 40 mW (estimated density of 4.3 W/cm$^2$), and the AOM was modulated with a 50% duty cycle at 1 MHz, such
528 that the time averaged power was 20 mW. Fluorescence was collected through the objective, separated with a
529 multi-wavelength imager (Photometrics, Dual-view), and imaged onto a water-cooled electron-multiplying charge
530 coupled device (Andor, iXon Ultra 888). Movies were collected for 2000 frames at 25 msec exposures with 2x
531 binning, 600 EM gain, 1x pre-amp gain, 30.0 MHz readout mode, 0.60 µs vertical speed, and +4 clock voltage
532 running at –67°C using the open source microscopy software Micro-Manger (Edelstein et al., 2014).

533 **smFRET Imaging Buffers.** VcINDY homodimers were imaged in the following buffers, which all contained 100
534 mM KCl, and 20 mM Tris-Cl ($pH_{25C}$=7.5). **Buffer LX**: 100 mM choline chloride. **Buffer LS**: 100 mM choline
535 chloride, and 1 mM succinic acid. **Buffer HX**: 100 mM NaCl. **Buffer HS**: 100 mM NaCl, and 1 mM succinic acid.
536 All buffers also contained 1% β-D-glucose, 1 mM trolox, 0.0025 U glucose oxidase, 0.02 U catalase, 1 mM
537 1,3,5,7-cyclooctatetraene, and 1 mM 3-nitrobenzyl alcohol as photostabilizing additives.

538 **smFRET Data Analysis.** Diffraction-limited spots of fluorescence intensity within the first 400 frames (10
539 seconds) were located in both the donor and acceptor fluorescence channels. Intensity versus time trajectories
540 were estimated using the iterative, maximum likelihood formulas for intensity estimation $N = \left(\sum_{xy}\left(d_{xy} - b\right)\Psi_{xy}\right)/$

541 $\left(\sum_{xy} \Psi_{xy}^2\right)$ and $b = \left(\sum_{xy}\left(d_{xy} - N\Psi_{xy}\right)\right)/\left(\sum_{xy} 1\right)$, where (x,y) is a pixel location, N is the fluorescence intensity, b
542 is the background intensity, and $\Psi$ is a fixed width, Gaussian-shaped point spread function with width defined by
543 the TIRF microscope optics. Donor and acceptor fluorescence channels were aligned using a 4th order
544 polynomial transform of ~2800 control points obtained from an image of an array of sub-diffraction limit
545 nanopatterned features localized in both channels. Trajectories were manually classified to select trajectories
546 from only donor-acceptor labeled molecules (see Fig. 1—Figure Supplement 1). The photobleaching point for
547 each $E_{FRET}$ trajectory was inferred using Bayesian inference (see below). A non-linear filter (Haran, 2004) was
548 applied to fluorescence intensity trajectories for easier visualization in intensity and $E_{FRET}$ trajectory plots, but all
549 analyses (*e.g.*, histograms, and HMMs) were performed using the unfiltered data.

550 **Global, variational Bayes hidden Markov modeling (vbHMM)**. Global vbHMMs were estimated in a manner
551 similar to a previously described single trajectory vbHMM implemented in the software package vbFRET
552 (Bronson et al., 2009). vbFRET is a Bayesian inference-based 'maximum evidence' method (Kinz-Thompson et
553 al., 2021), which allowed one to determine the simplest HMM that sufficiently accounts for the complexity of the
554 smFRET data (Bronson et al., 2009; van de Meent et al., 2014; Hon and Gonzalez, 2019). In this method, one
555 can find the most parsimonious HMM for smFRET data by estimating several HMMs, each with an increasing
556 number of hidden states, then calculating the 'evidence' for each HMM and choosing the one with the maximum
557 evidence value (Bronson et al., 2009). As seen in the directed acyclic graph (Fig. 4–Figure Supplement 1), the
558 only difference between vbFRET, and the global vbHMM used here is that an ensemble of $E_{FRET}$ versus time
559 trajectories is assumed to be independent and identically distributed (I.I.D.) from the same HMM parameters in
560 the global vbHMM model. Thus, all data points then contribute to the expectation and maximization equations
561 for the hyperparameters governing the posterior probability distribution, as opposed to only those from a single
562 trajectory is done for vbFRET. This is equivalent to considering one large, concatenated trajectory with vbFRET,
563 where however there is no conditional dependence for the hidden state on the previous hidden state for
564 neighboring data points from different trajectories. Instead, the first data point of each trajectory depends on the
565 initial-state probability distribution denoted here by π. As can be done with vbFRET, model selection can be
566 performed by calculating the evidence lower bound (ELBO) for each model and choosing that model with the
567 largest value.

568 To demonstrate the utility of using model selection with global vbHMMs, we simulated multiple four-state
569 time series, performed model selection, and compared this to an autocorrelation function (ACF) analysis (Fig.
570 4–Figure Supplement 2). The two-point autocorrelation function (Berne and Pecora, 2000) of a stationary
571 stochastic process or signal, y(t), describes how similar the process remains after some time lag, $\tau$, and can be
572 calculated as

573 $$ACF(\tau) \equiv \langle \delta y(0) \cdot \delta y(\tau) \rangle = \int_{-\infty}^{\infty} \int_{-\infty}^{\infty} d\delta y(0) \cdot d\delta y(t) \cdot y(0) \cdot y(\tau) \cdot P(\delta y(0), \delta y(\tau))$$

where $\delta y(\tau) = y(\tau) - \langle y \rangle$, angular brackets denote an expectation value, P(x) is the probability distribution function of x, and

$$P\big(\delta y(0), \delta y(\tau)\big) = P\big(\delta y(\tau) | \delta y(0)\big) \cdot P\big(\delta y(0)\big).$$

For a discrete, zero-mean signal, A(t), composed of N data points, the ACF can be estimated as

$$ACF(\tau) \equiv \langle A(0)A(\tau) \rangle = \lim_{N \to \infty} \frac{1}{N} \sum_{i=1}^{N} A_i A_{i+\tau}$$

Thus, assuming normally distributed values of $A_i A_{i+\tau}$, the ACF and the associated precision is distributed as a student-T distribution, $T_\nu(x|\mu, \sigma^2)$ with $\nu$ degrees of freedom, as $T_{N-1}(ACF(\tau)|\bar{x}, (\sum_i (x_i - \bar{x})^2)/(N(N-1)))$, where $x_i = A_i A_{i+\tau}$, and $\bar{x} = \frac{1}{N} \sum_i A_i A_{i+\tau}$. This is derived from the posterior marginal of a normal-distribution likelihood with a normal-gamma prior with $\kappa$=0, $\alpha$=–1/2, and $\beta$=0 (Murphy, 2007). The same formulas can be used to calculate an ACF from multiple signal trajectories that are independent and identically distributed; for instance the ACF at time $\tau$ would then include terms $A_i^0 A_{i+\tau}^0 + A_i^1 A_{i+\tau}^1 + \cdots + A_i^M A_{i+\tau}^M$ , where the superscript denotes an index over *M* number of signal trajectories. We refer to this as the ensemble ACF.

For some specific types of signals, we can calculate an analytical form of the ACF for comparison to observed ACFs. First, if a time-dependent signal was stationary at zero and distributed according to $y(t) \sim \mathcal{N}(0, \sigma^2)$, where $\mathcal{N}$ denotes a normal distribution, and $\sigma^2$ is the variance, the $ACF(t) = \sigma^2 \cdot \delta(t)$, where $\delta(t)$ is a Dirac delta function, which is one when t=0, and zero otherwise. Second, consider a zero-mean Markov chain with N states that are normally distributed according to $\mathcal{N}\big(\mu_i, \sigma_i^2\big)$ for the i$^{th}$ state, but where $\langle y \rangle = 0$. Also, consider that the rate constant for the transition from the i$^{th}$ state to the j$^{th}$ state, $k_{ij}$, can be written as a rate constant matrix, K, with the associated Q matrix (K but where the on-diagonals are the negative sum of the rate constants out the i$^{th}$ state). Notably, a vector of the probability of being in a particular state, P(t), given an initial probability vector, P(0), can then be written $P(t) = e^{Qt} \cdot P(0)$, where *e* denotes a matrix-exponential. If the Markov chain is in state i, the signal value at a particular time can be written $y(t) \sim \mu_i + N_i$, where $N_i \sim \mathcal{N}\big(0, \sigma_i^2\big)$. Thus, the ACF for this model is

$$\langle y(0)y(t) \rangle = \sum_i \sum_j \int_{N_i} \int_{N_j} (\mu_i + N_i)\big(\mu_j + N_j\big) \cdot P(j, t; i, 0; N_t; N_0),$$

where

$$P(j, t; i, 0; N_t; N_0) = P(j, t|i, 0) \cdot P_i(t = \infty) \cdot \mathcal{N}\big(0, \sigma_j^2\big) \cdot \mathcal{N}\big(0, \sigma_i^2\big).$$

Therefore

$$\langle y(0)y(t) \rangle = \sum_{i,j} \mu_i \mu_j \cdot d_j \cdot e^{Qt} \cdot d_i \cdot P_i(t = \infty) + \sum_i \sigma_i^2 \cdot P_i(t = \infty) \cdot \delta(t)$$

$$\equiv ACF_{MC}(t) + \langle \sigma^2 \rangle \cdot \delta(t),$$

where $d_i$ is a vector with a 1 in position i, and $ACF_{MC}$ is the contribution from the Markov chain. Additionally, we note that $P(j, t|i, 0) \cdot P(i) = d_j \cdot e^{Qt} \cdot d_i \cdot P_i(t = \infty)$ can be rewritten with a spectral expansion as $\sum_i C_i e^{-\lambda_i t}$,

605 where $C_i$ is a weighting factor, and $\lambda_i$ is an eigenvalue of $e^{Qt}$. Thus, for this Markov chain model with normally
606 distributed noise, the ACF can be written as a weighted sum of *N* exponential decays with a term at t=0
607 corresponding to the average amount of uncorrelated, normally distributed noise. Therefore, for this model, the
608 difference between ACF(t=0) and the next data point ACF(t=dt) is mostly $\langle\sigma^2\rangle$, and the rest of the ACF is
609 described by various exponential decays to zero.

610 In order to simulate single-molecule trajectories, we used the stochastic simulation algorithm (Gillespie,
611 1976) with the parameters in Table 1 with additive, normally distributed noise. From these 400 trajectories, we
612 estimated global HMMs with one through six states as described above. As expected, the HMM with four states
613 had the largest ELBO (Fig. 4–Figure Supplement 2). Additionally, we calculated the ACFs of these HMMs as
614 described above. Notably, of these ACFs, only those for HMMs with four or more states are sufficient to match
615 the individual and ensemble ACFs of the simulated trajectories (Fig. 4–Figure Supplement 2). Thus, the most
616 parsimonious global HMM determined by this method also recapitulates the kinetic results of a model-free ACF
617 method, but has the additional benefit as a model-based method of providing a mechanistic interpretation of
618 those results.

**Table 1.** $E_{FRET}$ trajectory simulation parameters

| Parameter | Value | Units |
|---|---|---|
| $\mu_1$ | 0.1 | A.U. |
| $\mu_2$ | 0.3 | A.U. |
| $\mu_3$ | 0.7 | A.U. |
| $\mu_4$ | 0.9 | A.U. |
| $k_{12}$ | 0.25 | $sec^{-1}$ |
| $k_{13}$ | 0.50 | $sec^{-1}$ |
| $k_{14}$ | 1.00 | $sec^{-1}$ |
| $k_{21}$ | 0.50 | $sec^{-1}$ |
| $k_{23}$ | 1.00 | $sec^{-1}$ |
| $k_{24}$ | 0.25 | $sec^{-1}$ |
| $k_{31}$ | 1.00 | $sec^{-1}$ |
| $k_{32}$ | 0.25 | $sec^{-1}$ |
| $k_{34}$ | 0.50 | $sec^{-1}$ |
| $k_{41}$ | 0.25 | $sec^{-1}$ |
| $k_{42}$ | 0.50 | $sec^{-1}$ |
| $k_{43}$ | 1.00 | $sec^{-1}$ |
| $\sigma$ | 0.20 | A.U. |
| $\tau$ | 0.01 | $sec$ |
| n | 2000 | frames |
| N | 400 | trajectories |

$\mu$ is an emission mean, $k$ is a rate constant, $\sigma$ is a standard deviation of additive noise, $\tau$ Is the time period of each data point, $n$ is the length of each trajectory, N is the number of trajectories

619 **Photobleaching detection**. We detect photobleaching by using shape-based Bayesian model selection to
620 choose the photobleaching time, or lack thereof, in a fluorescence intensity trajectory (Ray et al., 2021). Each
621 model, $M_T$, that we choose between is similar in that before some time, T, the data points are assumed to be
622 distributed according to a normal distribution with some mean, $\mu_1$, and some precision, $\lambda_1$ (i.e., inverse variance
623 $\lambda=\sigma^{-2}$), which we do not care about, while the data points after time T are distributed according to a normal
624 distribution with mean of zero, and some different precision, $\lambda_2$. We then calculate the probability of each $M_T$,

having marginalized out the means and precisions so that the conclusions are relevant regardless of those values, and then use Bayesian inference to select the $M_T$ that gives the best estimate of the photobleaching time as is supported by the available data. Practically, this method assigns all observed fluorescence at the beginning of a trajectory into the same 'on' state, usually with a large variance to account for different intensity states that compose the 'on' state, and then finds the last point where the data can be described as dropping to zero. For an ensemble of intensity trajectories, we perform model selection twice. The first time, we use uniform priors for the photobleaching time, while the second time, we use the independently calculated photobleaching times to infer an ensemble photobleaching rate constant, and then repeat the photobleaching time model selection calculation using this photobleaching rate constant to define the prior probability distribution for T for all of the independent intensity trajectories.

Mathematically, the likelihood for one of these models $M_T$ is

$$P(\{x\}|\mu_1,\lambda_1,\lambda_2,T) = \prod_{t<T} \mathcal{N}(x_t|\mu_1,\lambda_1^{-1}) \prod_{t\geq T} \mathcal{N}(x_t|0,\lambda_2^{-1}),$$

where $\mathcal{N}(x|\mu,\sigma^2)$ is a normal distribution with mean μ, and variance $\sigma^2$. Using a prior probability distribution of

$$\begin{aligned} P(\mu_1,\lambda_1,\lambda_2) &= NG(\mu_1,\lambda_1|\alpha_1,\beta_1,\kappa_1,m_1)\cdot G(\lambda_2|\alpha_2,\beta_2) \\ &= \left[(2\pi)^{-\frac{1}{2}}(\kappa_1\lambda_1)^{\frac{1}{2}} e^{-\frac{\kappa_1\lambda_1}{2}(\mu_1-m_1)^2}\cdot \beta_1^{\alpha_1}\Gamma(\alpha_1)^{-1}\lambda_1^{\alpha_1-1}\, e^{-\beta_1\lambda_1}\right]\cdot\left[\beta_2^{\alpha_2}\Gamma(\alpha_2)^{-1}\lambda_2^{\alpha_2-1}\, e^{-\beta_2\lambda_2}\right], \end{aligned}$$

where NG is a joint normal-gamma distribution, and G is a gamma distribution,(Murphy, 2007) we obtain a posterior probability distribution of the same form but with updated hyperparameters (denoted by primes)

$$P(\mu_1,\lambda_1,\lambda_2|\{x\},T) = NG(\mu_1,\lambda_1|\alpha_1',\beta_1',\kappa_1',m_1')\cdot G(\lambda_2|\alpha_2',\beta_2'),$$

where

$$\alpha_1' = \alpha_1 + T/2$$

$$\beta_1' = \beta_1 + \frac{1}{2}\sum_{i=0}^{T}(x_i - \langle x\rangle)^2 + \frac{\kappa_1 T(\langle x\rangle - m_1)^2}{2(\kappa_1+T)}$$

$$\kappa_1' = \kappa_1 + T$$

$$m_1' = \frac{\kappa_1 m_1 + T\langle x\rangle}{\kappa_1 + T}$$

$$\alpha_2' = \alpha_2 + (N-T)/2$$

$$\beta_2' = \beta_2 + \frac{1}{2}\sum_{i=T}^{N} x_i^2\,,$$

where N is the total number of data points. However, we do not particularly care about the exact values of $\mu_1$, $\lambda_1$, or $\lambda_2$, so instead, we can marginalize them out to find the probability that of the observed data given the model $M_T$ (i.e., the "evidence"), regardless of these nuisance parameters. In this case, we find

$$P(\{x\}|M_T) = P(\{x\}_{t<T}|M_T)\cdot P(\{x\}_{t\geq T}|M_T)$$

$$= \left[\frac{\Gamma(\alpha_1')}{\Gamma(\alpha_1)} \cdot \frac{\beta_1^{\alpha_1}}{\beta_1'^{\alpha_1'}} \cdot \left(\frac{\kappa_1}{\kappa_1'}\right)^{\frac{1}{2}} \cdot (2\pi)^{-\frac{T}{2}}\right] \cdot \left[\frac{\Gamma(\alpha_2')}{\Gamma(\alpha_2)} \cdot \frac{\beta_2^{\alpha_2}}{\beta_2'^{\alpha_2'}} \cdot (2\pi)^{-\frac{(N-T)}{2}}\right].$$

Now, with the evidence for the data given a photobleaching time, $P(\{x\}|M_T)$, we use Bayesian inference to select best photobleaching model (i.e., the model best supported by the data, regardless of the individual parameters) as the largest value of

$$P(M_T|\{x\}) = \frac{P(\{x\}|M_T) \cdot P(M_T)}{\sum_{T=0}^{N} P(\{x\}|M_T) \cdot P(M_T)}.$$

As discussed above, $P(M_T)$ is at first taken to be a constant and all trajectories are analyzed independently. Then, we infer the ensemble photobleaching rate constant using Bayesian inference with an exponential distribution as a likelihood, and a gamma distribution as the conjugate prior, and therefore also the posterior. As a result, we estimate $k_{PB} = (1+n)/(1+\sum_{i=0}^{n} T_i)$, where *i* indexes the different trajectories. Then, we use an exponential distribution as the prior $P(M_T) = k_{PB} e^{-k_{PB}T}$, where $k_{PB}$ is treated as a deterministic value. Finally, we note that these model selection calculations are performed in log-space, and that we subtract the maximum of all the log terms (i.e., scale by a constant) from both the numerator and denominator in order the to avoid computer underflow.

Since the models used for model selection in this algorithm are not comprehensive in the sense that they do not account for every experimental nuance of the data, we believe it is best to manually examine the selected model and the underlying fluorescence intensity trajectory to ensure that they are reasonably well matched, and so that one can manually adjust the photobleaching time when they do not match due to unaccounted for experimental behaviors (*e.g.*, deviations from Gaussian emissions).

**Calculation of Cycle Fluxes.** For the mechanistic scheme for transport in Fig. 5, the following terms are necessary to calculate cycle fluxes to be calculated. For shorter notation, we use $t \equiv k_t$, $d' \equiv k_d'$, $d'' = k_d''$,$A_o \equiv k_a'[A]_o^m$, $A_i \equiv k_a'[A]_i^m$, $B_o \equiv k_a''[B]_o^n$, and $B_i \equiv k_a''[B]_i^n$. The cycle flux for any cycle is

$$J_\kappa = J_{\kappa+} - J_{\kappa-} = (\Pi_{\kappa+} - \Pi_{\kappa-})\, \Sigma_\kappa/\Sigma,$$

where

$$\Pi_{a+} - \Pi_{a-} = t^2 d'(A_o - A_i),$$

$$\Pi_{b+} - \Pi_{b-} = t^2 d''(B_o - B_i),$$

$$\Pi_{c+} - \Pi_{c-} = t^2 d' d''(A_o B_o - A_i B_i),$$

$$\Sigma_a = 2td'' + d''^2,$$

$$\Sigma_b = t(A_o + A_i) + A_o A_i,$$

$$\Sigma_c = 1, \text{ and}$$

683 $\Sigma = 2t^3[d''(4d' + 2A_i + A_o) + (2A_iB_i + A_oB_o + A_oB_i + B_oA_i)]$

684 $+ 2t^2\big[d''^2(2d' + A_i + A_o)$

685 $+ d''\big((2(A_o + A_i) + (B_o + B_i) + 2d')d' + (A_iB_i + B_oA_i + 2A_oA_i + A_oB_o + A_oB_i)\big)$

686 $+ \big((A_oB_o + A_iB_i)d' + (A_oB_oA_i + A_oA_iB_i + A_oB_oB_i + B_oA_iB_i)\big)\big]$

687 $+ 2t\big[d''^2\big((A_o + A_i)d' + A_oA_i + d'^2\big) + d''\big((A_oB_o + A_iB_i)d' + (A_oB_oA_i + A_oA_iB_i)\big) + (A_oB_oA_iB_i)\big].$

688 From these equations, the functional form of $J_c$ for each first order rate constant, $k$, in Fig. 5 is $[ak + b + ck^{-1}]^{-1}$
689 where the coefficients *a*, *b*, and *c* depend on the other rate constants. This functional form has a maximum at
690 $k = \sqrt{c/a}$ , so there is an optimal value of $k_t$ that maximizes transport cycle flux under for a given set of substrate
691 concentrations. Finally, we note that $\Sigma$ has 90 terms, and thus so does $J_c$. Due to the changes to the energy
692 landscape in Fig. 6, 68 of the terms in $J_c$ increase the magnitude of $J_c$, 18 decrease it, and 4 do not change it.

693 To find the optimal parameters to describe previously published succinate transport data, a target energy
694 function of $\left(J^{expt} - (J_b + J_c)\right)^2$ was used for $J^{expt}([X] = K_M) = \frac{V_{max}}{2}$ and $J^{expt}([X] = 1000K_M) = V_{max}$ for the
695 sodium titration in their Figure 3 ($K_M = 41.7\,mM$, and $V_{max} = 53.5\,nmol\,mg^{-1}min^{-1} = 58.3\,s^{-1}$), and the
696 succinate titration in their Figure 6 ($K_M = 1.0\,\mu M$, and $V_{max} = 232.6\,nmol\,mg^{-1}min^{-1} = 253.4\,s^{-1}$) (Mulligan et
697 al., 2014). The collective energy function for both experiments was minimized using an affine invariant MCMC
698 ensemble sampler (Foreman-Mackey et al., 2013) with 200 walkers, a 1,000 step burn-in period, and a 10,000
699 step production period from which every 100th point was taken as a sample to avoid autocorrelation within the
700 samples.

701 The steady-state probability of apo VcINDY in Buffer HX was calculated from the mechanism in Fig. 5 by
702 setting $[B]_o = [B]_i = 0$, using the estimates for $k'_a$, $\langle k \rangle \equiv k_t$, and $k'_d$ (Fig. 5—Figure Supplement 2) and $[A]_o =$
703 $[A]_i = [Na^+] = 0.1M$, to calculate the steady state probability $P_{apo} = P_{C_o} + P_{C_i}$ as

704 $$P_{apo} = \frac{3\langle k \rangle^3 + k'_a[Na^+]^3\langle k \rangle^2}{3\langle k \rangle^3 + 4k'_a[Na^+]^3\langle k \rangle^2 + {k'_a}^2[Na^+]^6\langle k \rangle}.$$

705 **Crystallization of Wild Type VcINDY with Substrates**. Crystals of VcINDY were grown with a protein
706 concentration of 6 mg/ml at 4°C in hanging-drop vapor diffusion. For VcINDY-succinate, crystallization was
707 carried out with 30% PEG 300, 5 mM sodium succinate, 200 mM sodium chloride, and 100 mM MES pH 5.8.
708 VcINDY-fumarate crystals were grown with 37.5% PEG 300, 200 µM sodium fumarate, and 100 mM sodium
709 acetate pH 4.6. For VcINDY-malate, crystals were grown with 25% PEG 400, 20 mM sodium malate, and 100
710 mM sodium acetate pH 5.0.

711 **X-ray Data Collection and Structure Determination**. Crystals were frozen in liquid nitrogen with the
712 crystallization solution serving as the cryoprotectant. X-ray data were collected at the Advanced Photon Source
713 Beamlines 19-ID and 19-BM. Data processing and scaling were performed using the HKL2000 software
714 (Otwinowski and Minor, 1997). All crystals were of space group $P2_1$ with unit cell dimensions around a = 106 Å,

715 b = 102 Å, c = 171 Å, β = 99°, and contained four molecules per asymmetric unit. The structures were determined
716 by molecular replacement using the structure of VcINDY (PDB: 5UL9) (Nie et al., 2017) with sodium and citrate
717 removed as the initial search model, followed by repeated cycles of model building in Coot (Emsley and Cowtan,
718 2004), and refinement in Phenix (Table 2) (Adams et al., 2010).

719 **Data and Code Availability.** VcINDY structures with fumarate, malate, and succinate bound were deposited in
720 the PDB with IDs 6OKZ, 6OL0, and 6OL1, respectively. Code used to process smFRET data is described in a
721 separate manuscript (in preparation, C.D.K. and R.L.G.).

**Table 2.** X-ray crystallography of VcINDY in complex with substrate

| | Parameter | VcINDY-succinate | VcINDY-fumarate | VcINDY-malate |
|---|---|---|---|---|
| Data collection | Wavelength (Å) | 0.9791 | 0.9794 | 0.9794 |
| | Resolution range (Å) | 50.0-3.09 (3.15-3.09) | 50-3.29 (3.35-3.29) | 50.0-3.50 (3.56-3.50) |
| | Space group | $P2_1$ | $P2_1$ | $P2_1$ |
| | Cell dimensions: a, b, c (Å) | 105.5, 102.5, 171.1 | 105.8, 102.1, 171.2 | 106.8, 102.4, 171.8 |
| | Cell angle: $\beta$ (°) | 98.808 | 98.937 | 97.791 |
| | Total reflections | 128,621 (6,360) | 99,521 (3,598) | 86,871 (4,328) |
| | Unique reflections | 65,778 (3,229) | 51,510 (1,913) | 44,866 (2,248) |
| | Multiplicity | 5.0 (5.1) | 6.6 (5.3) | 6.9 (6.4) |
| | Completeness (%) | 99.9 (100) | 93.9 (71.0) | 96.4 (96.9) |
| | $I/\sigma(I)$ | 10.3 (0.625) | 10.1 (0.667) | 10.8 (0.571) |
| | Wilson B ($Å^2$) | 80.97 | 110.64 | 134.20 |
| | $R_{pim}$ | 8.4 (152) | 4.4 (54.2) | 3.5 (61.5) |
| | $CC_{1/2}$ | 0.998 (0.443) | 0.102 (0.512) | 0.997 (0.604) |
| Refinement | $R_{work}/R_{free}$ (%) | 25.3% / 29.6% | 24.9% / 28.5% | 26.1% / 30.5% |
| | No. atoms - Protein/Ligands | 13,325 / 40 | 13,097 / 23 | 12,792 / 42 |
| | RMSD bond lengths (Å) | 0.003 | 0.003 | 0.001 |
| | RMSD bond angles (°) | 0.66 | 0.52 | 0.39 |
| | Ramachandran favored (%) | 88.7 | 91.3 | 93.2 |
| | Ramachandran allowed (%) | 9.99 | 7.30 | 5.72 |
| | Ramachandran outliers (%) | 1.35 | 1.44 | 1.12 |
| | Rotamer outliers (%) | 0.07 | 0.0 | 0.0 |
| | Clashscore | 34.26 | 29.10 | 23.49 |

Numbers in parentheses are statistics for the highest resolution shell.

# 722 CRediT Authorship Contribution Statement

723 **Colin D. Kinz-Thompson:** Conceptualization, Methodology, Resources, Investigation, Validation, Formal
724 Analysis, Data Curation, Writing - Original Draft, Writing - Review & Editing, Visualization. **Marisa Lopez-**
725 **Redondo:** Methodology, Resources, Investigation, Validation. **Christopher Mulligan:** Investigation, Validation,
726 Formal Analysis, Visualization. **David B. Sauer:** Investigation, Validation, Formal Analysis, Data Curation,

Visualization. **Jennifer J. Marden:** Resources, Validation. **Jinmei Song:** Resources, Validation. **Emad Tajkhorshid:** Conceptualization, Writing - Review & Editing, Supervision, Project Administration, Funding Acquisition. **John F. Hunt:** Conceptualization, Methodology, Resources, Supervision, Funding Acquisition. **David L. Stokes:** Conceptualization, Methodology, Resources, Supervision, Funding Acquisition. **Joseph A. Mindell:** Conceptualization, Methodology, Resources, Data Curation, Writing - Review & Editing, Visualization, Supervision, Project Administration, Funding Acquisition. **Da-Neng Wang:** Conceptualization, Methodology, Resources, Data Curation, Writing - Review & Editing, Visualization, Supervision, Project Administration, Funding Acquisition. **Ruben L. Gonzalez, Jr.:** Conceptualization, Methodology, Resources, Data Curation, Writing - Review & Editing, Visualization, Supervision, Project Administration, Funding Acquisition.

# Acknowledgements

R.L.G. acknowledges support from the National Institutes of Health (NIH) through grants R01-GM084288 and R01-GM137608. D.N.W. acknowledges support from the NIH through grants R01-GM121994, R01-NS108151, and R01-DK099023, the G. Harold and Leila Y. Mathers Foundation, and the TESS Research Foundation. J.M. and C.M. acknowledge support from the National Institute of Neurological Disorders and Stroke (NINDS) Intramural Program, and C.M. acknowledges support from the Biotechnology and Biological Sciences Research Council through grant BB/V007424/1. D.L.S. acknowledges support from NIH through grant R35-GM144109. J.F.H. acknowledges support from NIH through grants R01-GM127883. E.T. acknowledges support from NIH through grants P41-GM104601 and R01-GM123455. D.B.S. acknowledges support, in part, from an American Cancer Society Postdoctoral Fellowship (PF-17-135-01) and from the Office of the Assistant Secretary of Defense for Health Affairs, through the Peer Reviewed Cancer Research Program under Award No. W81XH-16-1-0153. Crystal screening and X-ray data collection were carried out at NSLS-II Brookhaven National Laboratory and at Argonne National Laboratory, Structural Biology Center (SBC) at the Advanced Photon Source. SBC-CAT is operated by Univ. Chicago Argonne, LLC, for the U.S. Department of Energy, Office of Biological and Environmental Research under contract DE-AC02-06CH11357. Electron microscopy was performed at the NYU School of Medicine Microscopy Core.

# References

Adams PD, Afonine PV, Bunkóczi G, Chen VB, Davis IW, Echols N, Headd JJ, Hung L-W, Kapral GJ, Grosse-Kunstleve RW, McCoy AJ, Moriarty NW, Oeffner R, Read RJ, Richardson DC, Richardson JS, Terwilliger TC, Zwart PH. 2010. PHENIX: a comprehensive Python-based system for macromolecular structure solution. *Acta Crystallogr D Biol Crystallogr* **66**:213–221. doi:10.1107/S0907444909052925

Akyuz N, Altman RB, Blanchard SC, Boudker O. 2013. Transport dynamics in a glutamate transporter homologue. *Nature* **502**:114–118. doi:10.1038/nature12265

Bayburt TH, Sligar SG. 2010. Membrane protein assembly into Nanodiscs. *FEBS Lett* **584**:1721–1727. doi:10.1016/j.febslet.2009.10.024

Bergeron MJ, Clémençon B, Hediger MA, Markovich D. 2013. SLC13 family of $Na^+$-coupled di- and tri-carboxylate/sulfate transporters. *Mol Aspects Med* **34**:299–312. doi:10.1016/j.mam.2012.12.001

Berne BJ, Pecora R. 2000. Dynamic Light Scattering: With Applications to Chemistry, Biology, and Physics, Unabridged edition. ed. Mineola, N.Y: Dover Publications.

Bronson JE, Fei J, Hofman JM, Gonzalez RL, Wiggins CH. 2009. Learning rates and states from biophysical time series: a Bayesian approach to model selection and single-molecule FRET data. *Biophys J* **97**:3196–205. doi:10.1016/j.bpj.2009.09.031

Denisov IG, Grinkova YV, Lazarides AA, Sligar SG. 2004. Directed Self-Assembly of Monodisperse Phospholipid Bilayer Nanodiscs with Controlled Size. *J Am Chem Soc* **126**:3477–3487. doi:10.1021/ja0393574

Denisov IG, Sligar SG. 2017. Nanodiscs in Membrane Biochemistry and Biophysics. *Chem Rev* **117**:4669–4713. doi:10.1021/acs.chemrev.6b00690

Drew D, Boudker O. 2016. Shared Molecular Mechanisms of Membrane Transporters. *Annu Rev Biochem* **85**:543–72. doi:10.1146/annurev-biochem-060815-014520

Edelstein AD, Tsuchida MA, Amodaj N, Pinkard H, Vale RD, Stuurman N. 2014. Advanced methods of microscope control using μManager software. *J Biol Methods* **1**:10. doi:10.14440/jbm.2014.36

Emsley P, Cowtan K. 2004. Coot: model-building tools for molecular graphics. *Acta Crystallogr D Biol Crystallogr* **60**:2126–2132. doi:10.1107/S0907444904019158

Erkens GB, Hänelt I, Goudsmits JMH, Slotboom DJ, van Oijen AM. 2013. Unsynchronised subunit motion in single trimeric sodium-coupled aspartate transporters. *Nature* **502**:119–123. doi:10.1038/nature12538

Felle H, Porter JS, Slayman CL, Kaback HR. 1980. Quantitative measurements of membrane potential in Escherichia coli. *Biochemistry* **19**:3585–3590. doi:10.1021/bi00556a026

Fersht A. 2017. Structure and Mechanism in Protein Science: A Guide to Enzyme Catalysis and Protein Folding. WORLD SCIENTIFIC. doi:10.1142/10574

Fitzgerald GA, Mulligan C, Mindell JA. 2017. A general method for determining secondary active transporter substrate stoichiometry. *eLife* **6**:e21016. doi:10.7554/eLife.21016

Foreman-Mackey D, Hogg DW, Lang D, Goodman J. 2013. emcee: The MCMC Hammer. *Publ Astron Soc Pac* **125**:306–312. doi:10.1086/670067

Forrest LR, Krämer R, Ziegler C. 2011. The structural basis of secondary active transport mechanisms. *Biochim Biophys Acta Bioenerg* **1807**:167–188. doi:10.1016/j.bbabio.2010.10.014

Garaeva AA, Slotboom DJ. 2020. Elevator-type mechanisms of membrane transport. *Biochem Soc Trans* **48**:1227–1241. doi:10.1042/BST20200290

Gillespie DT. 1976. A general method for numerically simulating the stochastic time evolution of coupled chemical reactions. *J Comput Phys* **22**:403–434. doi:10.1016/0021-9991(76)90041-3

Haran G. 2004. Noise reduction in single-molecule fluorescence trajectories of folding proteins. *Chem Phys* **307**:137–145. doi:10.1016/j.chemphys.2004.05.017

Hill TL. 2005. Free energy transduction and biochemical cycle kinetics. Mineola, N.Y: Dover Publications.

Hon J, Gonzalez RL. 2019. Bayesian-Estimated Hierarchical HMMs Enable Robust Analysis of Single-Molecule Kinetic Heterogeneity. *Biophys J* **116**:1790–1802. doi:10.1016/j.bpj.2019.02.031

Jardetzky O. 1966. Simple allosteric model for membrane pumps. *Nature* **211**:969–970. doi:10.1038/211969a0

Kim JW, Kim Subin, Kim Songwon, Lee H, Lee J, Jin MS. 2017. Structural insights into the elevator-like mechanism of the sodium / citrate symporter CitS. *Sci Rep* **7**:2548. doi:10.1038/s41598

Kinz-Thompson CD, Ray KK, Gonzalez RL. 2021. Bayesian Inference: The Comprehensive Approach to Analyzing Single-Molecule Experiments. *Annu Rev Biophys* **50**:191–208. doi:10.1146/annurev-biophys-082120-103921

Lambert TJ. 2019. FPbase: a community-editable fluorescent protein database. *Nat Methods* **16**:277–278. doi:10.1038/s41592-019-0352-8

Lo C-J, Leake MC, Berry RM. 2006. Fluorescence Measurement of Intracellular Sodium Concentration in Single Escherichia coli Cells. *Biophys J* **90**:357–365. doi:10.1529/biophysj.105.071332

Lolkema JS, Slotboom DJ. 2019. Models to determine the kinetic mechanisms of ion-coupled transporters. *J Gen Physiol* **151**:369–380. doi:10.1085/jgp.201812055

Maity S, Trinco G, Buzón P, Anshari ZR, Kodera N, Ngo KX, Ando T, Slotboom DJ, Roos WH. 2022. High-speed atomic force microscopy reveals a three-state elevator mechanism in the citrate transporter CitS. *Proc Natl Acad Sci* **119**:e2113927119. doi:10.1073/pnas.2113927119

Mancusso R, Gregorio GG, Liu Q, Wang D-N. 2012. Structure and mechanism of a bacterial sodium-dependent dicarboxylate transporter. *Nature* **491**:1–6. doi:10.1038/nature11542

Markovich D. 2012. Sodium-Sulfate/Carboxylate Cotransporters (SLC13)Current Topics in Membranes. Elsevier. pp. 239–256. doi:10.1016/B978-0-12-394316-3.00007-7

Mulligan C, Fenollar-Ferrer C, Fitzgerald GA, Vergara-Jaque A, Kaufmann D, Li Y, Forrest LR, Mindell JA. 2016. The bacterial dicarboxylate transporter VcINDY uses a two-domain elevator-type mechanism. *Nat Struct Mol Biol* **23**:256–263. doi:10.1038/nsmb.3166

Mulligan C, Fitzgerald GA, Wang D-N, Mindell JA. 2014. Functional characterization of a $Na^+$-dependent dicarboxylate transporter from Vibrio cholerae. *J Gen Physiol* **143**:745–759. doi:10.1085/jgp.201311141

Murphy KP. 2007. Conjugate Bayesian analysis of the Gaussian distribution (Technical Report). University of British Columbia.

Nie R, Stark S, Symersky J, Kaplan RS, Lu M. 2017. Structure and function of the divalent anion/$Na^+$ symporter from Vibrio cholerae and a humanized variant. *Nat Commun* **8**:15009. doi:10.1038/ncomms15009

Otwinowski Z, Minor W. 1997. Processing of X-ray diffraction data collected in oscillation mode. *Methods Enzymol* **276**:307–326.

Ray KK, Verma AR, Gonzalez Jr RL, Kinz-Thompson CD. 2021. Inferring the shape of data: A probabilistic framework for analyzing experiments in the natural sciences. *ArXiv210912462 Phys Q-Bio*.

Ruan Y, Miyagi A, Wang X, Chami M, Boudker O, Scheuring S. 2017. Direct visualization of glutamate transporter elevator mechanism by high-speed AFM. *Proc Natl Acad Sci* **114**:1584–1588. doi:10.1073/pnas.1616413114

Sampson CDD, Fàbregas Bellavista C, Stewart MJ, Mulligan C. 2021. Thermostability-based binding assays reveal complex interplay of cation, substrate and lipid binding in the bacterial DASS transporter, VcINDY. *Biochem J* **478**:3847–3867. doi:10.1042/BCJ20210061

Sampson CDD, Stewart MJ, Mindell JA, Mulligan C. 2020. Solvent accessibility changes in a $Na^+$-dependent C4-dicarboxylate transporter suggest differential substrate effects in a multistep mechanism. *J Biol Chem* **295**:18524–18538. doi:10.1074/jbc.RA120.013894

Sauer DB, Marden JJ, Sudar JC, Song J, Mulligan C, Wang D-N. 2022a. Structural basis of ion – substrate coupling in the $Na^+$-dependent dicarboxylate transporter VcINDY. *Nat Commun* **13**:2644. doi:10.1038/s41467-022-30406-4

Sauer DB, Song J, Wang B, Hilton JK, Karpowich NK, Mindell JA, Rice WJ, Wang D-N. 2021. Structure and inhibition mechanism of the human citrate transporter NaCT. *Nature* **591**:157–161. doi:10.1038/s41586-021-03230-x

Sauer DB, Trebesch N, Marden JJ, Cocco N, Song J, Koide A, Koide S, Tajkhorshid E, Wang D-N. 2020. Structural basis for the reaction cycle of DASS dicarboxylate transporters. *eLife* **9**:e61350. doi:10.7554/eLife.61350

Sauer DB, Wang B, Sudar JC, Song J, Marden J, Rice WJ, Wang D. 2022b. The ups and downs of elevator-type di-/tricarboxylate membrane transporters. *FEBS J* **289**:1515–1523. doi:10.1111/febs.16158

Stein WD, Lieb WR. 1986. Transport and diffusion across cell membranes. Orlando: Academic Press.

van de Meent J-W, Bronson JE, Wiggins CH, Gonzalez RL. 2014. Empirical Bayes Methods Enable Advanced Population-Level Analyses of Single-Molecule FRET Experiments. *Biophys J* **106**:1327–1337. doi:10.1016/j.bpj.2013.12.055

855 # Figures

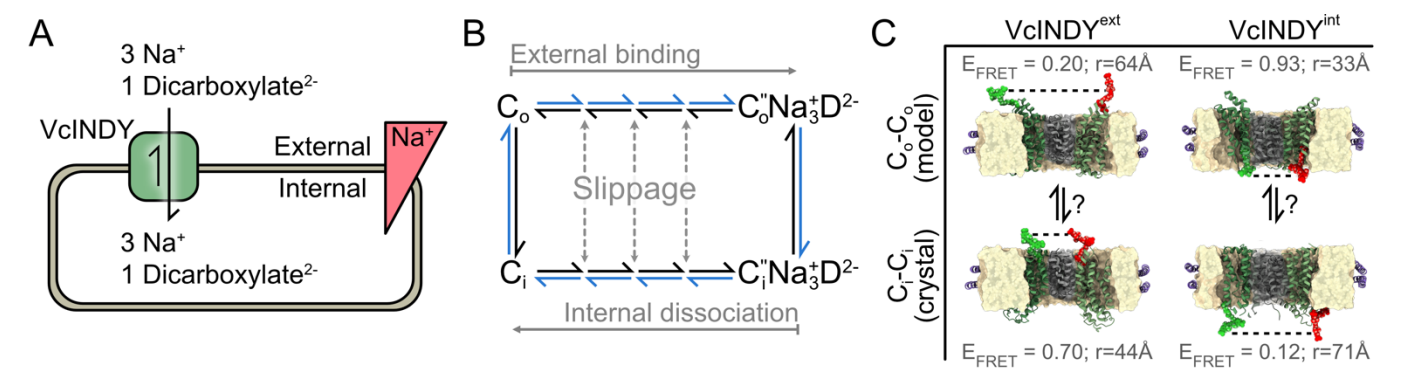


**Figure 1.** VcINDY transport cycle. (A) Diagram of VcINDY dimer (green) reversibly transporting sodium ions ($Na^+$) and dicarboxylate substrate ($D^{2-}$) into and out of a cell with a stoichiometry of 3:1; an inward facing $Na^+$ electrochemical gradient provides the free energy for vectorial transport. (B) Minimal mechanistic model of VcINDY transport cycle. Outward- and inward-facing conformations of the VcINDY homodimer ($C_o$, and $C_i$, respectively) bind $Na^+$ and $D^{2-}$ in an unknown order along the horizontal transitions; double-prime signifies both co-substrates are bound. VcINDY protomer conformational motions along the vertical transitions are involved in substrate translocation. At least one closed transport cycle, such as shown here in the clockwise direction in blue, is required for vectorial transport. Slippage reactions occur when an incomplete set of co-substrates is moved across the membrane. (C) Cartoon diagram of smFRET pairs designed to report on the VcINDY translocation reaction for $VcINDY^{ext}$ (left; G211) and $VcINDY^{int}$ (right; S436). The distance between each labeling position, *r*, was determined from the $C_\alpha$-$C_\alpha$ distance, and was measured for a $C_o$, substrate-bound repeat-swap model ($C_o$-$C_o$, PMDB: PM0080216), and a substrate-bound, $C_i$ X-ray crystallography structure ($C_i$-$C_i$, PDB: 5UL9). $E_{FRET}$ was estimated using $R_0$=51 Å. Scaffold domains are shown in gray, and transport domains are shown in green.

856

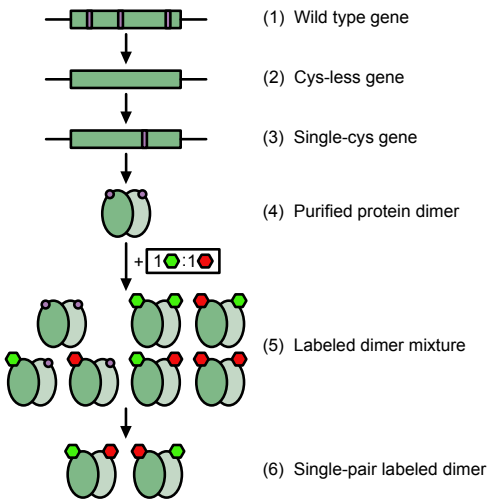


**Figure 1–Figure Supplement 1.** Cartoon schematic of approach to yield donor- and acceptor- fluorophore-labeled VcINDY homodimers. Site-directed mutagenesis is used to remove all codons encoding cysteine from a plasmid-based "wild type" VcINDY gene (1) to yield a "cys-less" variant (2), and used further to introduce a single codon encoding cysteine (3). This is over-expressed in *Escherichia coli* (*E. coli*), and purified to yield homodimers with single-cysteine containing protomers (4). The homodimers are labeled with a 1:1 ratio of maleimide-conjugated donor- and acceptor-fluorophores (5). Only those homodimers labeled with both a single donor- and single acceptor-fluorophore are computationally selected after imaging (6).

857

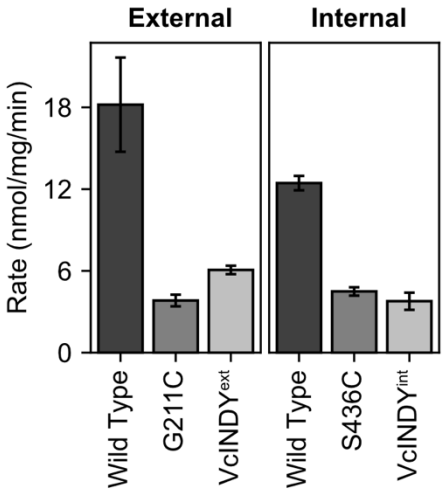


**Figure 1–Figure Supplement 2.** VcINDY biochemical transport assays. Transport rates of proteoliposome-embedded VcINDY homodimers for the external (left) and internal (right) smFRET pair labeled positions. Wild type (*i.e.*, cysteine-containing) assays were performed as control separately for each labeling position.

858

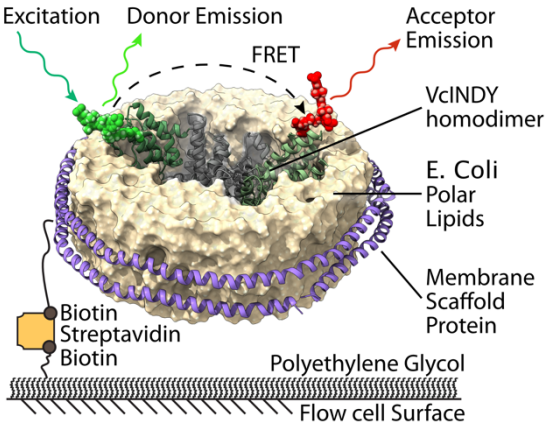


**Figure 2.** Schematic diagram of nanodisc-embedded VcINDY homodimer construct. Single cysteine mutant VcINDY labeled with a 1:1 ratio of donor and acceptor fluorophores is mixed with biotinylated membrane scaffold protein (MSP) and *E. coli* polar lipids to make nanodisc-embedded dimers. VcINDY containing nanodiscs are then tethered to a flow cell surface *via* a biotin-streptavidin-biotin bridge, and imaged using TIRF microscopy. The scaffold domains are shown in gray, and transport domains are shown in green.

859

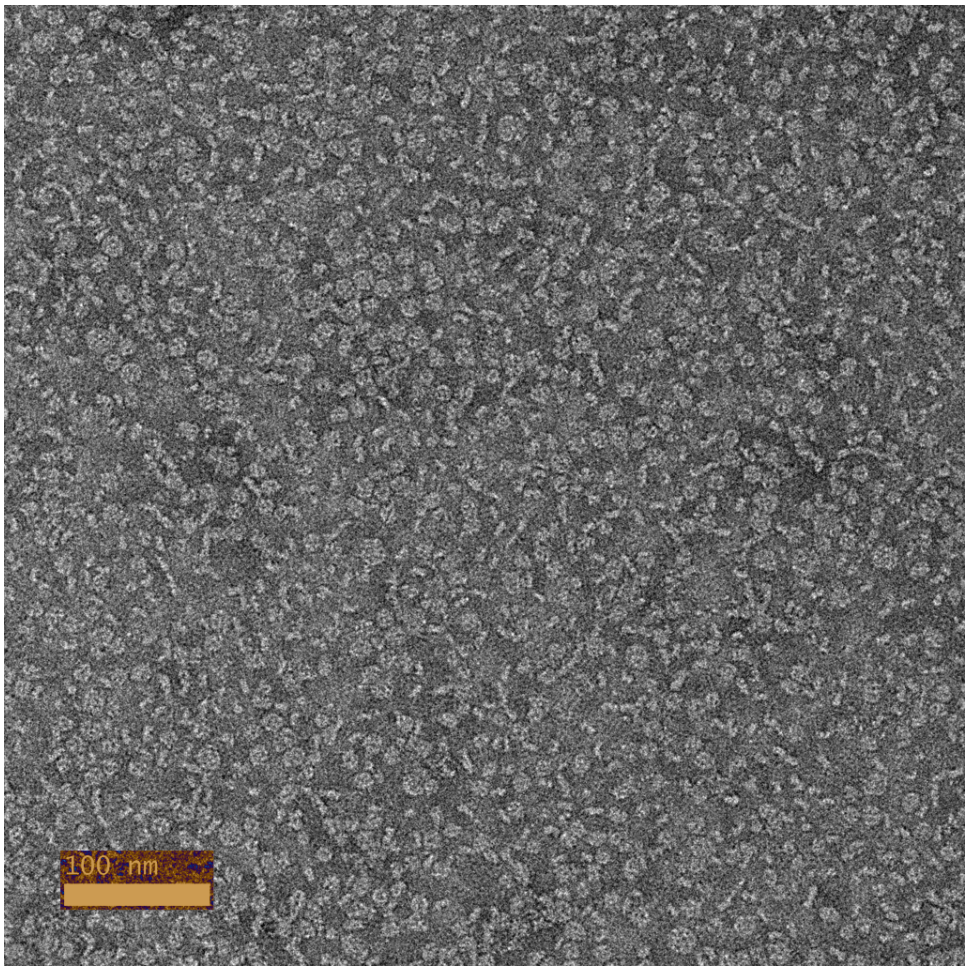


**Figure 2–Figure Supplement 1.** Negative stain electron microscopy of VcINDY reconstituted into lipid nanodiscs. Both top and side views of nanodiscs were seen. The nanodiscs had a diameter of ~108 Å and each contained one VcINDY dimer. The sample was uniform and no aggregation was observed.

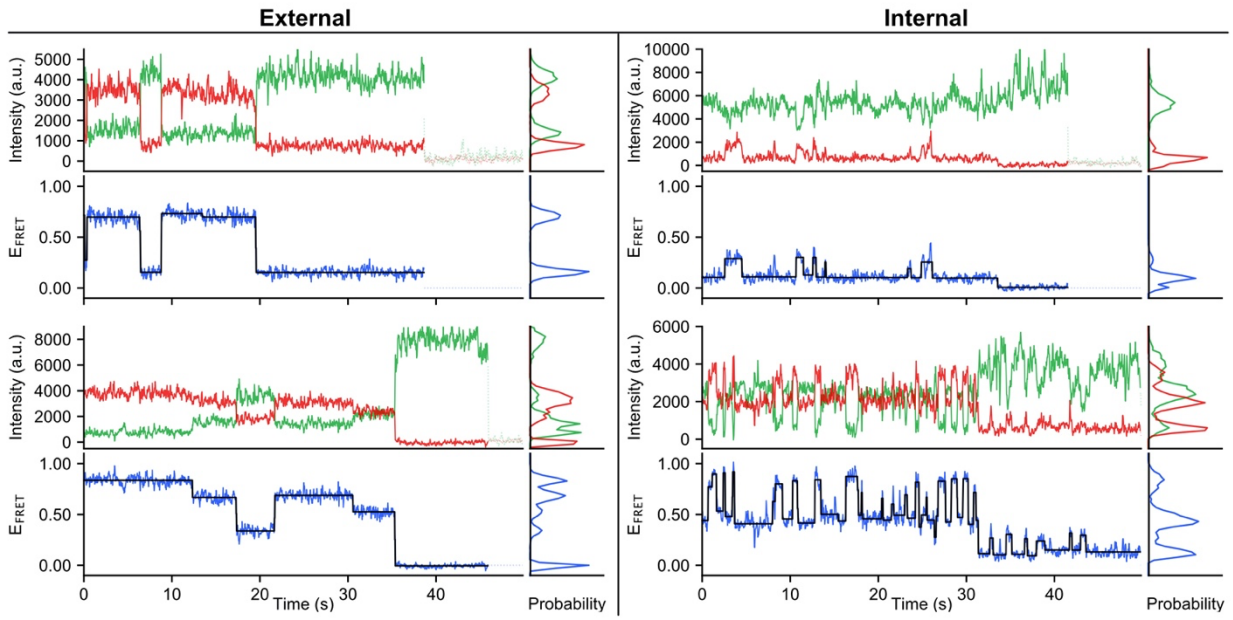


**Figure 3.** Equilibrium smFRET from VcINDY$^{ext}$ (left) and VcINDY$^{int}$ (right) in the presence of sodium and succinate (buffer HS). Example donor (green) and acceptor (red) fluorescence intensity trajectories, with corresponding $E_{FRET}$ trajectories (blue) and idealized trajectories (black) are shown. Several trajectories shown include donor fluorescence intensity after the acceptor fluorophore has photobleached, but this was removed prior to further analysis.

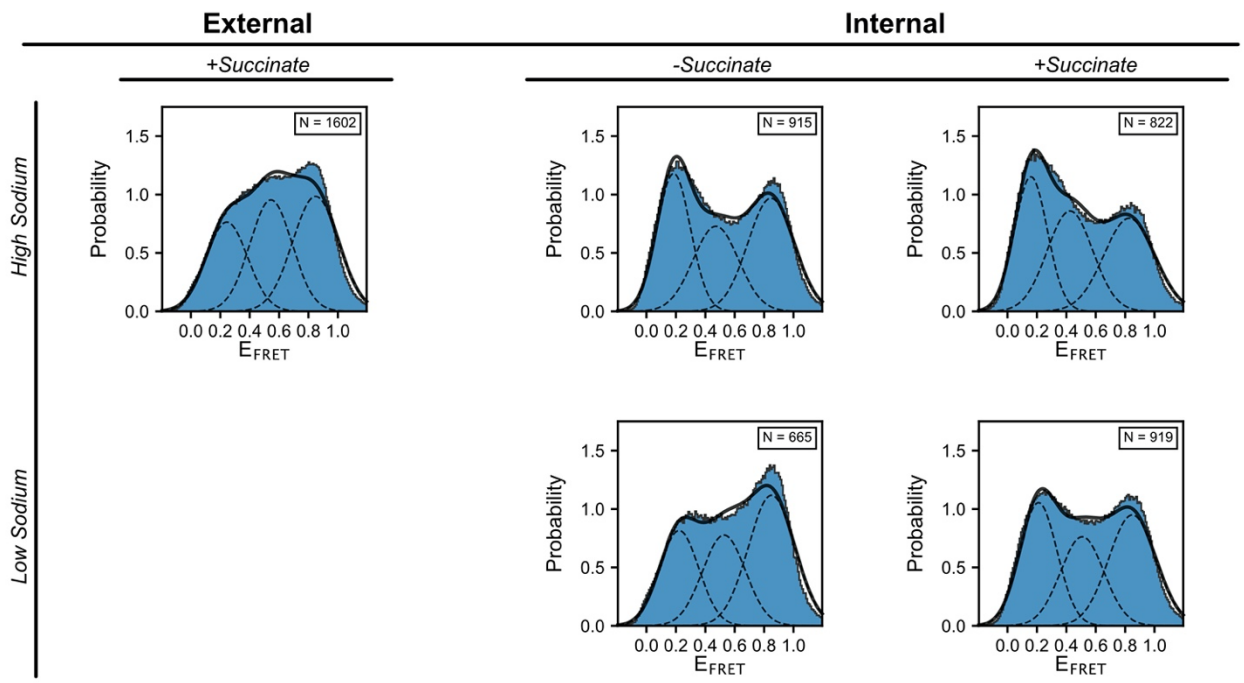


**Figure 4.** Substrate dependence of VcINDY $E_{FRET}$ distributions. Histograms of $E_{FRET}$ values from all external (left) and internal (right) smFRET signals recorded with VcINDY$^{ext}$, and VcINDY$^{int}$, respectively, in different buffer conditions. The $E_{FRET}$ data in these histograms were not filtered, and $E_{FRET}$ values corresponding to donor photobleaching have been removed (*i.e.*, the last dwell in an $E_{FRET}$ state of zero). The predictive posterior probability distribution for $E_{FRET}$ from the global HMM with the maximum ELBO is shown overtop (solid black) as a heuristic measure of how well the global HMM explains the entirety of each dataset, but this ignores the kinetic aspects of the HMM. The distributions for the individual, consensus $E_{FRET}$ states from the global HMM are shown as black dashed lines.

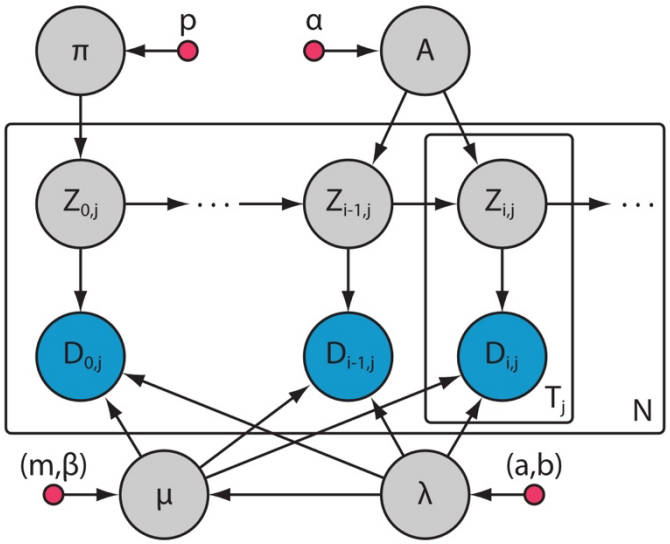


**Figure 4–Figure Supplement 1.** Directed acyclic graph for a global, variational Bayes HMM. Pink nodes represent hyperparameters, grey nodes represent unobserved variables, and blue nodes represent observed variables. $T_j$ is the number of data points in the $j^{th}$ trajectory, and $D_{i,j}$ corresponds to the $i^{th}$ data point of the $j^{th}$ trajectory. Arrows represent conditional dependencies.

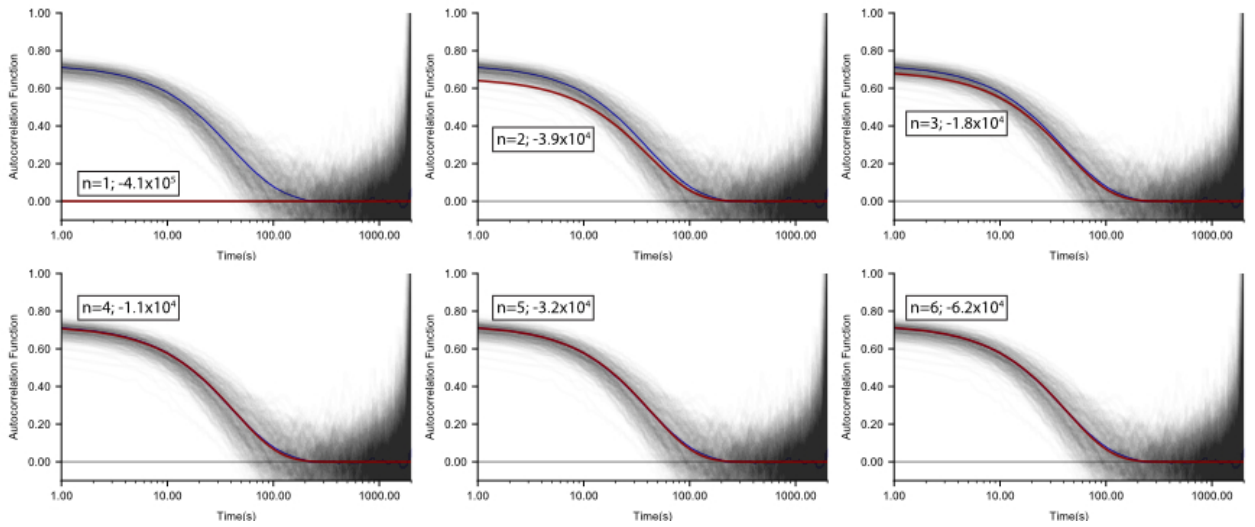


**Figure 4–Figure Supplement 2.** Autocorrelation function analysis of global HMMs with various number of hidden states of simulated, four-state $E_{FRET}$ trajectories. Individual ACFs (black), ensemble ACF (blue), and global HMM ACF (red). The maximum ELBO HMM (n=4; ln(ELBO)= $-1.1 \times 10^4$) matches the number of $E_{FRET}$ states in the simulation.

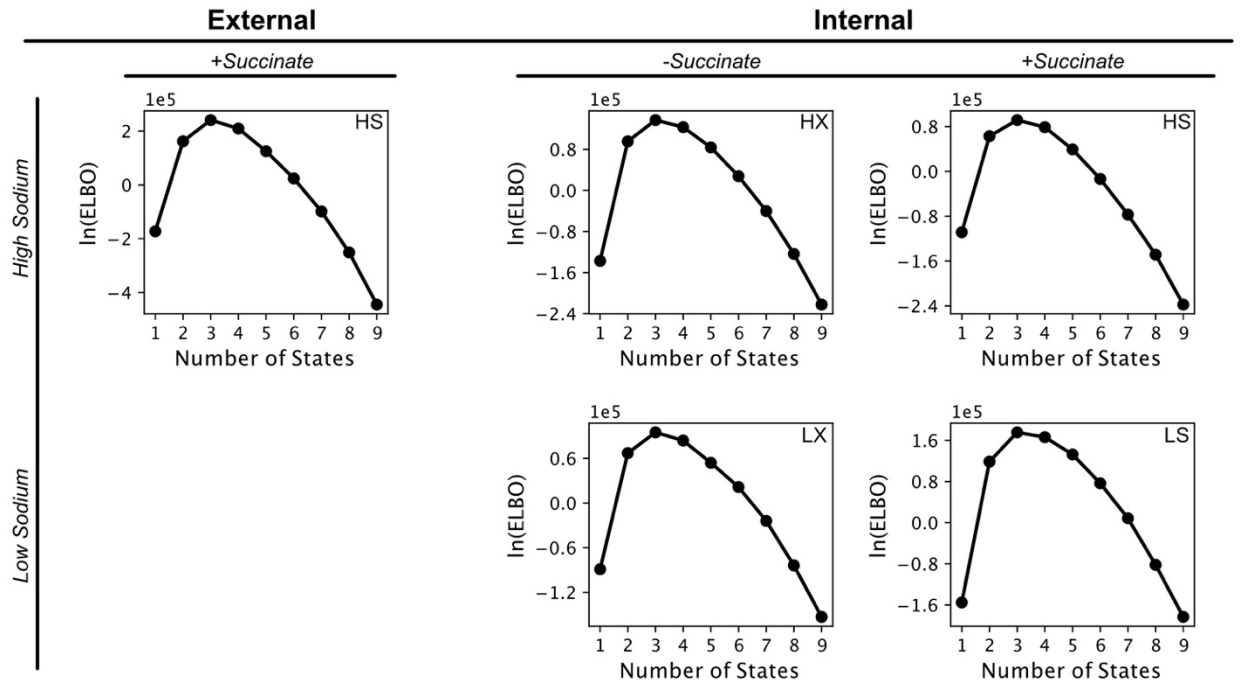


**Figure 4–Figure Supplement 3.** Substrate dependence of evidence lower bound (ELBO) calculations for global HMMs of VcINDY smFRET experiments. The maximum ELBO model is the HMM that best represents the set of $E_{FRET}$ trajectories for those substrate conditions.

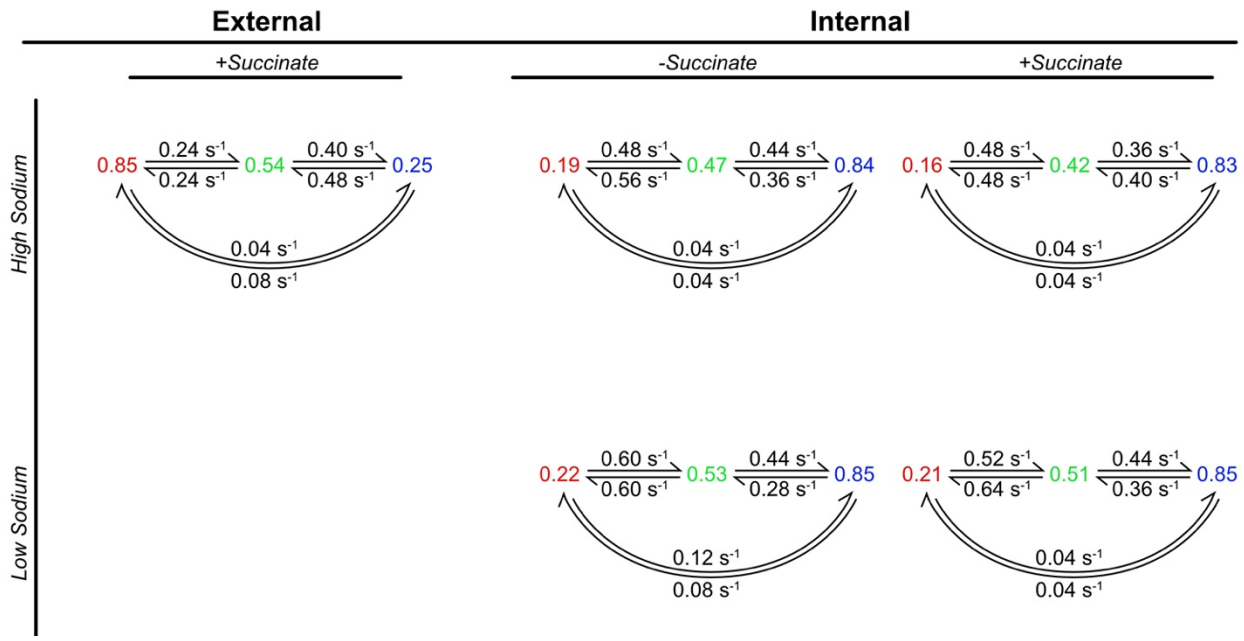


**Figure 4–Figure Supplement 4.** Substrate dependence of the HMM with maximum ELBO for global HMMs of VcINDY smFRET experiments. For each kinetic scheme, states are denoted by the mean $E_{FRET}$ value of that state, which was inferred from the HMM. Rate constants for transitions between states are shown above the arrows.

866

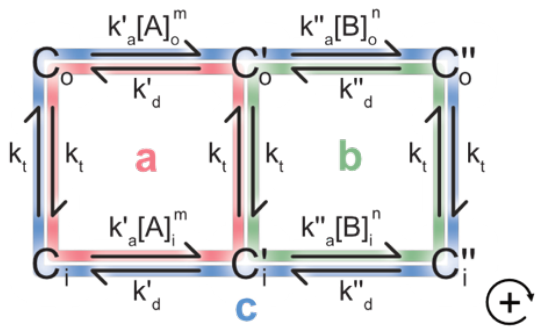


**Figure 5.** Free energy transduction model for a secondary active transporter. First order and pseudo-first order rate constants for the parsimonious kinetic model discussed in the text are given over each transition. For simplicity, co-substrate binding has been reduced to a strictly sequential, two-step process with mirror symmetry (Stein and Lieb, 1986). Substrate A is the first co-substrate to bind with stoichiometry $m$; co-substrate B binds second with stoichiometry $n$. Prime signifies the first co-substrate is bound; double-prime signifies both co-substrates are bound; $C_o$ and $C_i$ denote the outward and inward facing conformation of the transporter. $k_t$ is the translocation rate constant, $k_a$ is a second order association rate constant, and $k_d$ is a dissociation rate constant. Cycles *a* (red) and *b* (green) are responsible for slippage, while cycle *c* (blue) is responsible for transport. The positive direction is defined to be clockwise.

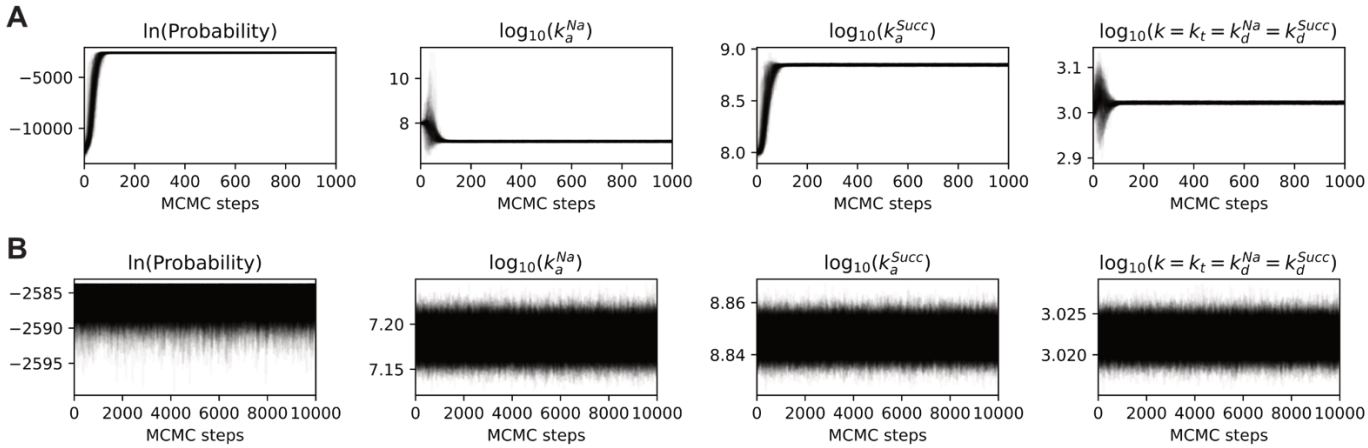


**Figure 5—Figure Supplement 1.** MCMC trajectories for optimal kinetic model parameters of VcINDY proteoliposome-based succinate transport assay. (A) Affine invariant ensemble MCMC sampler trajectories for 200 walkers during burn-in period. These samples were discarded. (B) Production period trajectories from 200 walkers. Only every 100th sample of those shown here was used to minimize autocorrelation.

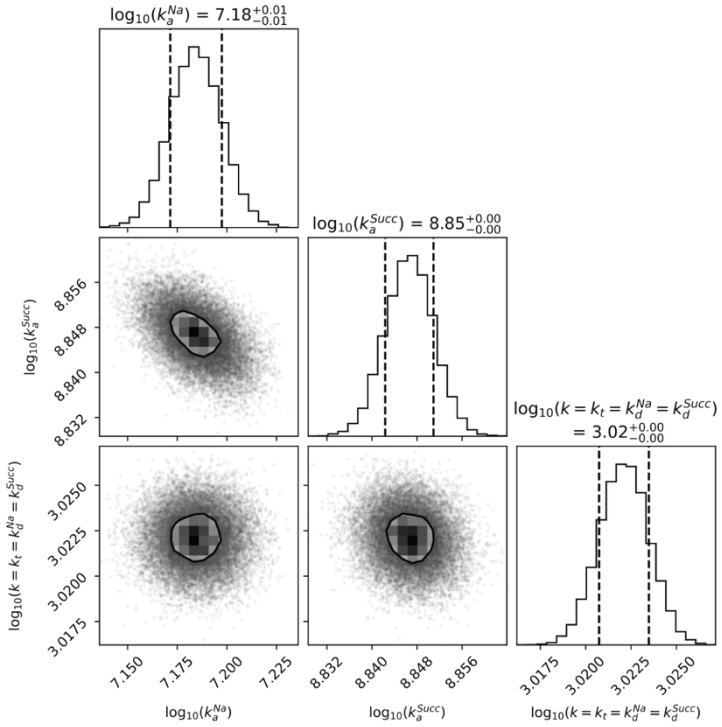


**Figure 5—Figure Supplement 2.** Corner plot of MCMC samples for optimal kinetic model parameters of VcINDY proteoliposome-based succinate transport assay. Ranges given are the $1\sigma$ level containing 39.3% of the sample volume.

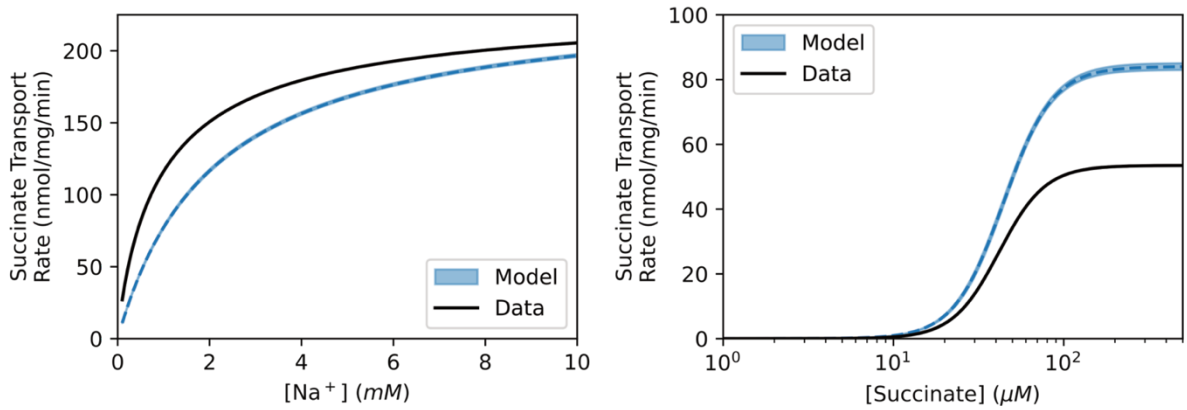


**Figure 5—Figure Supplement 3.** Modeled VcINDY transport rate experiments. Data from Mulligan and coworkers were reproduced from their reported $K_M$, $V_{max}$, and Hill coefficients (Mulligan et al., 2014). Modeled data are the 95% credible intervals generated from MCMC samples of $k_a'$, $k_a''$, and $\langle k \rangle$, and dashed lines are the lowest energy solution.

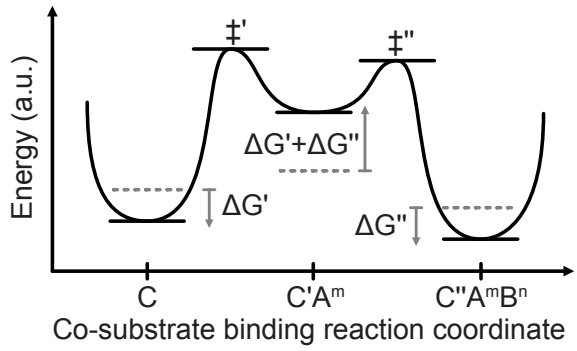


**Figure 6.** Schematic of optimized energy landscape for binding co-substrates A and B. Original energy levels are denoted with dashed lines for apo- ($C$), partially bound ($C'$), and fully bound ($C''$) transporter. Direction of perturbations to energy levels by amounts $\Delta G'$ and $\Delta G''$ are shown with arrows. Relative positioning of unperturbed $C$, $C'$, and $C''$, and transition states ‡ ′ and ‡ ″ are arbitrarily chosen, as are the magnitudes of $\Delta G'$ and $\Delta G''$.

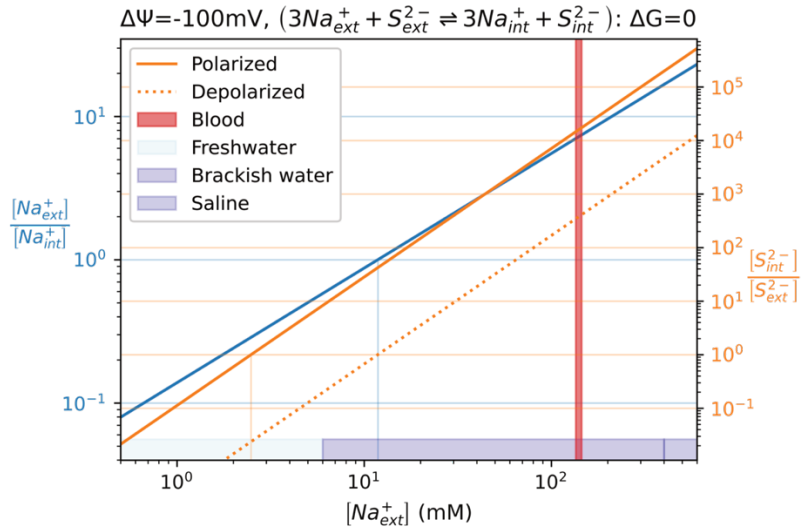


**Figure 6—Figure Supplement 1.** Estimated physiological $Na^+$ and succinate concentrations in a bacterial cell in different environments. External (ext) and internal (int) $Na^+$ concentrations were measured for another gammaproteobacteria, *E. coli*, at pH=7 (Lo et al., 2006). For *E. coli* at pH=7, the membrane potential difference ($\Delta\psi$) is approximately -100 mV (Felle et al., 1980). With these numbers, balancing the chemical potential difference and effects of charge for the VcINDY transport reaction at equilibrium provides the internal to external ratio of succinate concentrations for the cell (orange). When $\Delta\psi = 0$, the cell is depolarized (dashed).

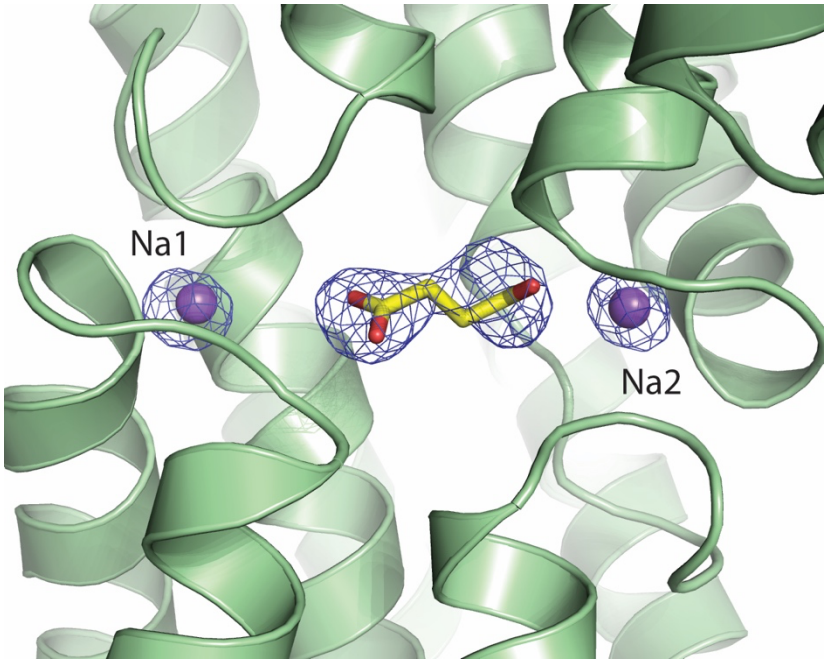


**Figure 7.** View of the VcINDY binding pocket from the cytosol. The X-ray crystallography derived structural model is of succinate- and $Na^+$-bound VcINDY (green). Electron density for the substrates is shown contoured at 2.5σ.

873